The Astrophysical Journal, 773:92 (21pp), 2013 August 20 doi:10.1088/0004-637X/773/2/92

AN *XMM-NEWTON* SURVEY OF THE SOFT X-RAY BACKGROUND. III. THE GALACTIC HALO X-RAY EMISSION

David B. Henley and Robin L. Shelton
Department of Physics and Astronomy, University of Georgia, Athens, GA 30602, USA; dbh@physast.uga.edu
Received 2013 February 20; accepted 2013 June 8; published 2013 July 29

ABSTRACT

We present measurements of the Galactic halo's X-ray emission for 110 *XMM-Newton* sight lines selected to minimize contamination from solar wind charge exchange emission. We detect emission from few million degree gas on ∼4/5 of our sight lines. The temperature is fairly uniform (median = 2.22×10^6 K, interquartile range = 0.63×10^6 K), while the emission measure and intrinsic 0.5–2.0 keV surface brightness vary by over an order of magnitude (∼(0.4–7) × 10^{-3} cm^{-6} pc and ∼(0.5–7) × 10^{-12} erg cm^{-2} s^{-1} deg^{-2}, respectively, with median detections of 1.9×10^{-3} cm^{-6} pc and 1.5×10^{-12} erg cm^{-2} s^{-1} deg^{-2}, respectively). The high-latitude sky contains a patchy distribution of few million degree gas. This gas exhibits a general increase in emission measure toward the inner Galaxy in the southern Galactic hemisphere. However, there is no tendency for our observed emission measures to decrease with increasing Galactic latitude, contrary to what is expected for a disk-like halo morphology. The measured temperatures, brightnesses, and spatial distributions of the gas can be used to place constraints on models for the dominant heating sources of the halo. We provide some discussion of such heating sources, but defer comparisons between the observations and detailed models to a later paper.

Key words: Galaxy: halo – ISM: structure – X-rays: diffuse background – X-rays: ISM

Online-only material: color figures

1. INTRODUCTION

Observations of the ∼0.1–1 keV diffuse soft X-ray background (SXRB; e.g., McCammon & Sanders 1990) show that ∼(1–3) × 10^6 K plasma is present in the halo of the Milky Way (Burrows & Mendenhall 1991; Wang & Yu 1995; Pietz et al. 1998; Wang 1998; Snowden et al. 1998, 2000; Kuntz & Snowden 2000; Smith et al. 2007b; Galeazzi et al. 2007; Henley & Shelton 2008; Lei et al. 2009; Yoshino et al. 2009; Gupta et al. 2009; Henley et al. 2010). The presence of this hot plasma is confirmed by the observation of zero-redshift O VII and O VIII absorption lines in the X-ray spectra of active galactic nuclei (AGNs; Nicastro et al. 2002; Fang et al. 2003, 2006; Rasmussen et al. 2003; McKernan et al. 2004; Williams et al. 2005; Bregman & Lloyd-Davies 2007; Yao & Wang 2007; Yao et al. 2008; Hagihara et al. 2010; Sakai et al. 2012; Gupta et al. 2012). The extent and mass of this hot gas are disputed: Gupta et al. (2012) argue that its extent is $\gtrsim$100 kpc and that it contains a significant fraction of the Galaxy's baryonic mass (see also Fang et al. 2013), while Wang & Yao (2012, and references therein) argue that the scale height of the hot gas is only a few kpc, in which case it would contribute a negligible amount to the Galaxy's baryons (Fang et al. 2013).

The origin of this hot halo gas is uncertain. Two main processes are thought to play a role in heating the halo. The first is supernova (SN) driven outflows from the Galactic disk (e.g., Shapiro & Field 1976; Bregman 1980; Norman & Ikeuchi 1989; Joung & Mac Low 2006). In such an outflow, the material may subsequently fall back to the disk in a so-called galactic fountain. The second process is accretion of material from the intergalactic medium (e.g., Toft et al. 2002; Rasmussen et al. 2009; Crain et al. 2010). However, the relative importance of these two processes is not well known.

Henley et al. (2010, hereafter HSKJM) tested models of the hot halo gas using a sample of 26 SXRB spectra extracted from archival *XMM-Newton* observations between $l = 120°$ and 240° (Henley & Shelton 2010, hereafter HS10). They compared the observed X-ray temperatures and emission measures of the hot halo with the distributions expected from different physical models. HSKJM's analysis favored fountains of hot gas (Joung & Mac Low 2006) as a major, possibly dominant, contributor to the halo X-ray emission in the *XMM-Newton* band over extraplanar SN remnants (Shelton 2006). However, in the absence of X-ray surface brightness predictions from disk galaxy formation models, they were unable to rule out the possibility that an extended halo of accreted material also contributed to the observed emission (Crain et al. 2010).

Here, we expand upon HSKJM's observational analysis, analyzing ∼4 times as many sight lines. Our observations are drawn from a new *XMM-Newton* SXRB survey which spans the full range of Galactic longitudes (Henley & Shelton 2012, hereafter HS12), and which supersedes the HS10 survey from which the HSKJM sample was drawn. As in HSKJM, our observations were selected because they should be less affected by solar wind charge exchange (SWCX) emission (Cravens 2000; Robertson & Cravens 2003; Koutroumpa et al. 2006)—time-variable X-ray line emission which arises within the solar system from charge exchange reactions between solar wind ions and neutral H and He (Cravens et al. 2001; Wargelin et al. 2004; Snowden et al. 2004; Koutroumpa et al. 2007; Fujimoto et al. 2007; Kuntz & Snowden 2008; Henley & Shelton 2008; HS10; Carter & Sembay 2008; Carter et al. 2010, 2011; Ezoe et al. 2010, 2011). In a separate paper, we will use these observations to test models of the hot halo gas (D. B. Henley et al., in preparation).

The remainder of this paper is organized as follows. In Section 2, we describe the observation selection and data reduction. In Section 3, we describe our spectral analysis method. We present the results in Section 4. We discuss and summarize our results in Sections 5 and 6, respectively.

2. OBSERVATIONS

2.1. Observation Selection

The observations that we analyze here are a subset of those analyzed by HS12, who extracted SXRB O VII and O VIII intensities from 1880 archival *XMM-Newton* observations spread across the sky. In order to minimize SWCX contamination, we apply various filters to the data (HSKJM). In particular, to minimize contamination from geocoronal SWCX and near-Earth heliospheric SWCX, we only use the portions of the *XMM-Newton* observations during which the solar wind proton flux was low or moderate. If excising the periods of high solar wind proton flux from an *XMM-Newton* observation resulted in too little usable observation time, the observation was rejected (see Section 2.4 of HS12). After this solar wind proton flux filtering, 1003 observations are usable (HS12, Table 2). We apply additional filters to these observations as follows. We minimize heliospheric SWCX contamination by using only observations toward high ecliptic latitudes ($|\beta| > 20^\circ$) taken during solar minimum (after 00:00UT on 2005 June 1[1]). As we are interested in the Galactic halo, we use only observations toward high Galactic latitudes ($|b| > 30^\circ$), and exclude observations toward the Magellanic Clouds, the Eridanus Enhancement (Burrows et al. 1993; Snowden et al. 1995), and the Scorpius-Centaurus (Sco-Cen) superbubble (Egger & Aschenbach 1995). Note that although we do not explicitly exclude the observations identified as being SWCX-contaminated by Carter et al. (2011, Table A.1), none of these observations are in our final sample.

The above criteria result in 163 observations being selected from HS12's original set of 1003. The observation IDs, names of the original targets,[2] and pointing directions for these 163 observations are shown in Columns 2–5 of Table 1 (Columns 6–9 contain additional observation information (Section 2.2) and Columns 10–15 contain the spectral fit results (Section 4)). If the original target was a bright X-ray source, we excised it from the data, since our goal is to measure the diffuse SXRB emission in each *XMM-Newton* field (see Section 2.2). Note that these 163 observations represent fewer than 163 different sight lines. If a set of observations are separated by less than $0.^\circ1$, we group them into a single sight line, and then fit our spectral model (Section 3.1) to all the observations simultaneously. In such cases, the observations for a given sight line are listed in the table on and below the row containing the sight line number (e.g., the results for sight line 20 were obtained by simultaneously fitting to the spectra from observations 0400920201 and 0400920101).

Our set of 163 observations includes a cluster of 28 observations near $(l, b) \approx (326^\circ, -58^\circ)$. These observations represent 27 different sight lines, which we have numbered 103.1–103.27 (sight line 103.8 consists of two observations). In order to avoid oversampling this region of the sky in our subsequent analysis, we treat these 27 sight lines as a single sight line, whose halo temperature and emission measure are found from the weighted means of the halo temperatures and emission measures of the individual sight lines. We tabulate these mean values as the results for sight line 103 in Columns 12 and 13 of Table 1. Similarly, the Galactic coordinates for this sight line are the means of the longitudes and latitudes for the individual sight lines. The subsequent analysis will use the mean results for sight line 103.

After grouping together observations of the same sight line, and combining the results from sight lines 103.1 through 103.27 as described above, our set of 163 observations yields 110 measurements of the halo's temperature and emission measure. The locations of our sight lines on the sky are shown in Figure 4, below.

Note that our sample of observations includes 20 of the 26 observations analyzed in HSKJM. Of the remaining six observations, five (0200960101, 0303260201, 0303720201, 0303720601, 0306370601) are excluded due to our using a later date to define the beginning of the solar minimum phase. The sixth observation (0305290201) is not included in HS12's catalog, and so is not included here, as it exhibits strong residual soft proton contamination (see Section 3.5 of HS12). Observations 0306060201 and 0306060301 were analyzed independently in HSKJM, but here they are grouped together (sight line 43).

2.2. Data Reduction

The data reduction is described in Section 2 of HS12 (see also Section 3 of HS10). Here, we give an overview of the process. The data reduction was carried out using the *XMM-Newton* Extended Source Analysis Software[3] (*XMM*-ESAS; Kuntz & Snowden 2008; Snowden & Kuntz 2011), as included in version 11.0.1 of the *XMM-Newton* Science Analysis Software[4] (SAS). Note that we re-extracted all the EPIC-MOS spectra from scratch for the current analysis, using a lower source removal flux threshold than in HS12 (see below).

Each observation was first processed with the SAS `emchain` script to produce a calibrated events list for each exposure. Then, the *XMM*-ESAS `mos-filter` script was used to identify and excise periods within each exposure that were affected by soft proton flaring. As indicated above, periods of high solar wind proton flux ($>2 \times 10^8$ cm^{-2} s^{-1}) were also removed from the data. The usable MOS1 and MOS2 exposure times that remain after this filtering are shown in Columns 6 and 8 of Table 1, respectively.

Because our goal is to measure the diffuse Galactic halo emission, we removed bright sources from the *XMM-Newton* data. As described in HS10 (Section 3.3) and HS12 (Section 2.2), we identified and removed bright and/or extended sources that would not be adequately removed by the automated source removal (described below). If the source to be removed was the original observation target, we centered the exclusion region on the target's coordinates; otherwise, the exclusion region was positioned by eye. In all cases we used circular exclusion regions. We chose the radii of these regions by eye, although in some cases we used surface brightness profiles to aid us. As noted in HS10 and HS12, we erred on the side of choosing larger exclusion regions, at the expense of reducing the number of counts in the SXRB spectra.

In general, we used the same source exclusion regions that we used in HS10 and HS12. These were chosen from a visual inspection of broadband X-ray images, which had undergone

[1] This date, taken from HS12, was estimated using sunspot data from the National Geophysical Data Center (http://www.ngdc.noaa.gov/stp/SOLAR/). Note that this date is later than the one used in HSKJM, as HS12 defined an "Intermediate" phase of the solar cycle between solar maximum and solar minimum. We did not define an end date for the solar minimum phase, as the sunspot data imply that this phase lasted at least until the most recent observation in the HS12 catalog (carried out on 2009 November 3–4).

[2] In general, the target names were obtained from the FITS file headers. If the target name was abbreviated or truncated, we attempted to determine the full name of the target from SIMBAD (http://simbad.u-strasbg.fr/simbad/). For a small number of targets, we were unable to determine the full name.

[3] http://heasarc.gsfc.nasa.gov/docs/xmm/xmmhp_xmmesas.html

[4] http://xmm.esac.esa.int/sas/

Table 1
Observation Details and Spectral Fit Results

Sight line	ObsID	Target	l (deg)	b (deg)	$t_1^{\rm exp}$ (ks)	Ω_1 (arcmin^2)	$t_2^{\rm exp}$ (ks)	Ω_2 (arcmin^2)	F/g R12 rate[a]	$N_{\rm H}$ (10^{20} cm^{-2})	Halo T (10^6 K)	Halo EM (10^{-3} cm^{-6} pc)	χ^2/dof	$S_{0.5-2.0}$[b]
(1)	(2)	(3)	(4)	(5)	(6)	(7)	(8)	(9)	(10)	(11)	(12)	(13)	(14)	(15)
1	0302580501	RX J2359.5−3211	5.676	−77.683	20.0	378	20.7	462	440	1.18	$1.77^{+0.15}_{-0.11} \pm 0.05$	$6.76^{+1.23\ +0.90}_{-1.18\ -0.86}$	513.03/434	$3.58^{+0.81}_{-0.77}$
2	0550460801	IC 5179	6.479	−55.914	24.9	373	25.4	454	652	1.39	$2.42^{+0.30\ +0.32}_{-0.19\ -0.11}$	$2.23^{+0.64\ +0.56}_{-0.63\ -0.58}$	484.98/541	$2.14^{+0.81}_{-0.82}$
3	0304080501	H 2356−309	12.896	−78.051	16.9	353	17.0	370	426	1.44	$2.10^{+0.11}_{-0.10} \pm 0.05$	$5.49^{+0.85\ +0.61}_{-0.79\ -0.74}$	391.39/355	$4.21^{+0.80}_{-0.83}$
4	0556210301	SDSS J163408.64+331242.0	54.428	+42.051	10.4	465	11.3	475	441	1.70	$3.42^{+6.36\ +4.64}_{-1.07\ -0.65}$	$0.77^{+0.84\ +0.42}_{-0.56\ -0.37}$	357.93/384	$1.00^{+1.21}_{-0.86}$
5	0505880101	SDSS J163246.54+340526.1	55.564	+42.457	13.5	342	14.6	492	447	1.73	$2.11^{+0.23\ +0.09}_{-0.28\ -0.07}$	$2.38^{+0.88}_{-0.83} \pm 0.58$	324.86/380	$1.84^{+0.81}_{-0.79}$
6	0505010501	J162636.39+350242.0	56.664	+43.826	10.7	378	12.3	526	456	1.43	$1.76^{+0.36\ +0.06}_{-0.34\ -0.05}$	$3.26^{+0.79}_{-1.62} \pm 0.71$	311.52/366	$1.70^{+0.55}_{-0.92}$
7	0504100401	SDSS 1437+3634	62.380	+65.692	7.9	407	8.1	493	682	1.06	$2.18^{+0.29\ +0.08}_{-0.34\ -0.07}$	$2.91 \pm 1.01^{+0.59}_{-0.51}$	330.93/321	$2.37^{+0.95}_{-0.92}$
8	0556212601	SDSS 163306.12+401747.5	63.988	+42.878	6.3	343	5.6	575	576	1.07	$2.15^{+0.84\ +0.11}_{-0.75\ -0.08}$	$1.71^{+1.76}_{-1.10} \pm 0.46$	227.97/236	$1.36^{+1.45}_{-0.95}$
9	0502510301	4C 32.44	67.149	+81.034	18.6	407	18.8	484	643	1.19	$2.78^{+0.89\ +1.81}_{-0.70\ -0.52}$	$0.81 \pm 0.47^{+0.62}_{-0.48}$	371.71/462	$0.90^{+0.86}_{-0.74}$
10	0501621601	3C 349	72.954	+38.208	8.7	399	8.8	492	483	1.88	$2.24^{+0.50\ +0.16}_{-0.41\ -0.10}$	$1.99^{+1.10\ +0.67}_{-1.04\ -0.59}$	274.32/303	$1.70^{+1.10}_{-1.02}$
11	0305361601	IRAS 13279+3401	73.737	+79.307	23.9	474	24.2	491	654	0.910	$2.13^{+0.40\ +0.17}_{-0.41\ -0.09}$	$1.23^{+0.64\ +0.43}_{-0.51\ -0.42}$	427.00/522	$0.97^{+0.61}_{-0.52}$
12	0212480701	GB 1428+4217	75.906	+64.905	13.5	378	13.5	531	600	1.15	$1.68^{+0.30}_{-0.24} \pm 0.05$	$3.78^{+1.53\ +0.80}_{-1.26\ -0.73}$	390.82/379	$1.72^{+0.79}_{-0.66}$
13	0551020901	51 Peg	90.085	−34.722	41.1	396	42.8	552	315	4.21	$2.70^{+0.31\ +0.19}_{-0.28\ -0.14}$	$2.30^{+0.67}_{-0.61} \pm 0.37$	528.77/594	$2.49^{+0.83}_{-0.77}$
14	0502500101	3C 457	92.525	−38.187	10.3	406	10.3	493	304	5.22	$2.80^{+0.74\ +0.15}_{-0.47\ -0.24}$	$1.30^{+0.57\ +0.22}_{-0.52\ -0.36}$	294.58/329	$1.45^{+0.68}_{-0.70}$
15	0304850901	NGC 253	96.866	−87.971	10.4	232	10.4	361	415	1.42	$2.02 \pm 0.14 \pm 0.05$	$6.12^{+1.97\ +0.70}_{-1.24\ -0.56}$	201.21/218	$4.38^{+1.50}_{-0.98}$
16	0404050301	3C 305	103.190	+49.106	6.3	473	6.4	564	584	1.31	2.1[c]	$0.00^{+0.90\ +0.02}_{-0.00\ -0.00}$	255.97/267	<0.69
17	0303420101	M 51	104.889	+68.578	31.9	202	31.7	306	626	1.82	$1.68^{+0.32}_{-0.31} \pm 0.05$	$2.43^{+2.56\ +0.74}_{-1.03\ -0.77}$	438.25/432	$1.12^{+1.22}_{-0.59}$
18	0405080501	NGC 5055	106.062	+74.293	6.4	302	6.7	449	569	1.29	$1.44^{+0.46\ +0.10}_{-0.61\ -0.05}$	$4.50^{+31.29\ +0.99}_{-3.06\ -1.53}$	193.49/199	$1.26^{+8.79}_{-0.96}$
19	0411980501	XMMSL1 J132342.3+482701	108.730	+67.786	6.3	404	6.3	495	627	0.934	$2.42^{+0.49\ +0.38}_{-0.42\ -0.15}$	$1.63^{+1.02\ +0.57}_{-0.82\ -0.51}$	189.13/207	$1.57^{+1.12}_{-0.93}$
20	0400920201	NGC 6217	111.311	+33.345	10.3	290	10.3	445	462	3.90	$2.50^{+0.25}_{-0.31} \pm 0.21$	$2.20^{+1.31\ +0.83}_{-0.56\ -0.37}$	535.81/563	$2.22^{+1.57}_{-0.67}$
	0400920101	NGC 6217	111.311	+33.346	8.8	356	9.2	444	...	...	...	...	...	...
21	0556230101	PG 1351+640	111.925	+52.021	10.6	300	10.5	519	898	1.98	2.1[c]	$0.25^{+0.59\ +0.02}_{-0.25\ -0.14}$	543.37/576	<0.64
	0556230201	PG 1351+640	111.924	+52.023	7.6	362	7.4	520	...	...	...	...	...	...
22	0405690501	NGC 5204 X-1	113.457	+58.007	15.5	390	15.4	402	867	1.75	2.1[c]	$0.69^{+0.51\ +0.36}_{-0.38\ -0.25}$	1052.66/967	$0.53^{+0.48}_{-0.35}$
	0405690201	NGC 5204 X-1	113.460	+58.010	29.3	379	33.5	403	...	...	...	...	...	...
23	0305360501	IRAS F12509+3122	116.949	+86.010	13.5	471	13.3	557	515	1.35	$2.08^{+0.14\ +0.06}_{-0.19\ -0.18}$	$3.26^{+0.71\ +0.71}_{-0.61\ -0.57}$	344.40/376	$2.45^{+0.75}_{-0.63}$
24	0413380601	RX J1257.0+4738	120.207	+69.447	5.0	455	5.2	478	640	1.23	$2.20^{+0.31\ +0.24}_{-0.28\ -0.07}$	$1.56^{+0.68\ +0.13}_{-0.55\ -0.53}$	578.19/614	$1.29^{+0.57}_{-0.63}$
	0551090101	RX J1257.0+4738	120.126	+69.460	14.1	397	14.0	479	...	...	...	...	...	...
25	0404980101	NGC 4736	123.290	+76.012	37.1	376	37.8	392	603	1.24	$2.33^{+0.29\ +0.30}_{-0.20\ -0.12}$	$1.66^{+0.51\ +0.53}_{-0.48\ -0.55}$	627.89/587	$1.51^{+0.67}_{-0.66}$
26	0304070501	NVSS J124638+564921	124.223	+60.304	11.8	398	11.9	488	743	0.790	$2.83^{+1.06\ +0.58}_{-0.75\ -0.37}$	$0.62^{+0.52\ +0.38}_{-0.43\ -0.25}$	339.65/321	$0.70^{+0.72}_{-0.56}$
27	0554500101	NGC 4686	124.481	+62.583	16.2	469	16.4	496	715	1.35	2.1[c]	$0.00^{+0.66\ +0.28}_{-0.00\ -0.00}$	397.70/458	<0.55
28	0401210601	NGC 3516	133.225	+42.419	17.5	267	16.9	352	593	3.45	$2.03^{+0.70\ +0.11}_{-0.62\ -0.06}$	$1.47^{+1.40}_{-1.14} \pm 0.48$	381.74/356	$1.06^{+1.07}_{-0.90}$
29	0502940301	RBS 797	135.043	+36.037	10.3	298	10.0	448	516	2.28	2.1[c]	$0.17^{+0.66\ +0.36}_{-0.17\ -0.17}$	303.06/292	<0.71
30	0404220101	PN G135.9+55.9	135.974	+55.981	12.6	393	13.5	477	606	1.72	2.1[c]	$0.16^{+0.74\ +0.49}_{-0.16\ -0.16}$	361.63/382	<0.80
31	0400560301	NGC 4258	138.279	+68.853	50.1	347	50.9	369	643	1.60	$2.19^{+0.19\ +0.11}_{-0.16\ -0.08}$	$2.10 \pm 0.53^{+0.48}_{-0.42}$	658.75/594	$1.73^{+0.59}_{-0.56}$
32	0504100901	SDSS J115704.83+524903.9	140.811	+62.383	5.6	332	5.4	565	624	1.88	$1.57^{+0.15}_{-0.45} \pm 0.05$	$4.31^{+9.31\ +1.07}_{-1.38\ -0.87}$	229.60/211	$1.60^{+3.47}_{-0.61}$

Table 1
(Continued)

Sight line	ObsID	Target	l	b	t_1^{exp}	Ω_1	t_2^{exp}	Ω_2	F/g R12	N_H	Halo T	Halo EM	χ^2/dof	$S_{0.5-2.0}$[b]
			(deg)	(deg)	(ks)	(arcmin^2)	(ks)	(arcmin^2)	rate[a]	(10^{20} cm^{-2})	(10^6 K)	(10^{-3} cm^{-6} pc)		
(1)	(2)	(3)	(4)	(5)	(6)	(7)	(8)	(9)	(10)	(11)	(12)	(13)	(14)	(15)
33	0560590201	M 82 ULX	141.420	+40.547	11.5	208	12.6	316	595	5.05	$3.00^{+0.58\ +0.21}_{-0.40\ -0.16}$	$1.96 \pm 0.82^{+0.17}_{-0.32}$	662.05/584	$2.30^{+0.98}_{-1.03}$
	0560590301	M 82 ULX	141.428	+40.549	14.0	224	14.6	317	...	...	...	...	...	...
34	0504101001	SDSS 1136+5657	141.982	+57.293	20.5	387	20.6	470	611	0.976	$3.60^{+8.15\ +8.51}_{-1.21\ -0.76}$	$0.39^{+0.41\ +0.28}_{-0.27\ -0.02}$	430.14/478	$0.52^{+0.67}_{-0.36}$
35	0504390201	Holmberg II X-1	142.330	+37.420	21.2	233	21.5	444	551	3.79	$4.04^{+2.16\ +0.05}_{-1.18\ -0.63}$	$0.53^{+0.60\ +0.14}_{-0.32\ -0.03}$	504.21/454	$0.78^{+0.91}_{-0.47}$
36	0400570201	SDSS J110912.39+612346.6	142.370	+51.705	22.2	448	22.3	461	586	0.642	$2.37^{+0.86\ +0.69}_{-0.36\ -0.17}$	$1.05^{+0.61\ +0.48}_{-0.55\ -0.42}$	443.20/492	$0.97^{+0.72}_{-0.64}$
37	0504101401	SDSS 1147+5226	143.936	+61.973	12.5	389	13.9	547	623	1.55	2.1[c]	$0.41^{+0.89\ +0.40}_{-0.41\ -0.38}$	352.34/417	<1.06
38	0502430701	RX J0957.8+6534	145.828	+43.062	8.6	394	9.2	539	638	5.31	2.1[c]	$0.00^{+0.42\ +0.39}_{-0.00\ -0.00}$	779.84/903	<0.44
	0502430201	RX J0957.8+6534	145.830	+43.062	38.1	325	40.6	538	...	...	...	...	...	...
39	0554120701	Lockman Hole	148.499	+51.426	12.8	394	14.7	545	569	0.707	$2.12^{+0.28\ +0.19}_{-0.29\ -0.09}$	$0.91^{+0.29\ +0.29}_{-0.26\ -0.37}$	1595.62/1982	$0.71^{+0.32}_{-0.35}$
	0554121301	Lockman Hole	148.476	+51.459	35.4	468	35.9	485	...	...	...	...	...	...
	0554120101	Lockman Hole	148.487	+51.462	22.6	393	24.3	486	...	...	...	...	...	...
	0554121001	Lockman Hole	148.484	+51.462	13.0	391	12.7	551	...	...	...	...	...	...
40	0606320401	NGC 4051	148.917	+70.070	15.3	361	15.6	441	684	1.15	$2.20^{+0.45\ +0.46}_{-0.13\ -0.08}$	$1.43^{+0.44\ +0.30}_{-0.43\ -0.41}$	1725.95/1543	$1.18^{+0.44}_{-0.49}$
	0606321401	NGC 4051	148.921	+70.071	14.6	295	15.1	440	...	...	...	...	...	...
	0606321901	NGC 4051	148.926	+70.074	19.3	292	21.9	439	...	...	...	...	...	...
	0606322201	NGC 4051	148.932	+70.076	8.3	292	8.3	370	...	...	...	...	...	...
41	0556211201	SDSS 104114.18+590219.4	149.033	+50.968	8.0	476	8.3	477	567	0.750	$1.57^{+0.60\ +8.11}_{-0.69\ -0.05}$	$1.65^{+8.43\ +0.47}_{-0.82\ -1.21}$	283.72/294	$0.62^{+3.16}_{-0.55}$
42[d]	0406630201	Abell 959	151.186	+48.245	7.7	265	8.0	412	577	1.00	2.1[c]	$0.00^{+1.35}_{-0.00} \pm 0.00$	104.58/104	<1.04
43	0306060301	NGC 4013	151.831	+70.103	15.0	380	15.5	467	687	1.26	$1.72^{+0.14}_{-0.09} \pm 0.05$	$3.20^{+0.58\ +0.54}_{-0.69\ -1.30}$	905.22/982	$1.55^{+0.38}_{-0.71}$
	0306060201	NGC 4013	151.829	+70.103	53.0	376	54.2	467	...	...	...	...	...	...
44	0553880201	NGC 4244	154.517	+77.171	25.6	478	26.9	497	598	1.89	$2.19 \pm 0.26^{+0.64}_{-0.08}$	$1.32^{+0.41\ +0.15}_{-0.31\ -0.57}$	838.43/973	$1.08^{+0.36}_{-0.53}$
	0553880301	NGC 4244	154.514	+77.171	12.1	404	12.0	496	...	...	...	...	...	...
45	0551200301	SDSS J094820.38+582526.6	155.329	+45.507	22.5	345	25.0	351	609	1.26	2.1[c]	$0.17^{+0.65\ +0.26}_{-0.17\ -0.17}$	499.50/485	<0.66
46	0504101301	SDSS 1123+4703	158.152	+63.571	17.6	401	17.7	482	677	1.36	2.1[c]	$0.57^{+0.85\ +0.35}_{-0.57\ -0.38}$	357.35/462	<1.14
47	0556214801	SDSS J094811.89+551726.4	159.477	+46.743	8.4	401	8.3	480	603	1.05	$2.00^{+0.28\ +0.05}_{-0.40\ -0.07}$	$2.01^{+1.56\ +0.68}_{-0.90\ -0.49}$	262.44/292	$1.42^{+1.20}_{-0.72}$
48	0500940201	RX J1011.0+5339	159.718	+50.442	9.3	329	9.4	551	597	0.754	$1.99^{+0.32\ +11.92}_{-0.52\ -0.05}$	$1.32^{+1.44\ +0.50}_{-0.86\ -0.68}$	261.43/310	$0.92^{+1.07}_{-0.76}$
49	0556214701	SDSS J093759.43+542427.3	161.392	+45.658	8.2	400	8.2	476	611	1.83	$2.44^{+0.56\ +0.28}_{-0.37\ -0.14}$	$1.72^{+1.01\ +0.12}_{-0.81\ -0.45}$	264.20/281	$1.67^{+1.00}_{-0.90}$
50	0502020101	Abell 222/223	162.597	−72.142	20.6	195	22.2	327	335	1.53	$2.10^{+0.35\ +0.12}_{-0.39\ -0.17}$	$1.43^{+1.25\ +0.43}_{-0.59\ -0.64}$	595.72/494	$1.09^{+1.01}_{-0.66}$
	0502020201	Abell 222/223	162.512	−72.072	5.4	150	5.3	337	...	...	...	...	...	...
51	0556213401	SDSS J104537.69+484914.5	162.661	+57.453	10.2	408	10.3	560	661	1.34	$2.34^{+1.30\ +0.61}_{-0.67\ -0.18}$	$0.85^{+0.72\ +0.63}_{-0.70\ -0.44}$	314.00/348	$0.77^{+0.87}_{-0.75}$
52[d]	0502220301	APM 08279+5255	165.745	+36.257	9.1	416	8.9	498	605	4.11	2.1[c]	$0.13^{+0.66\ +0.08}_{-0.13\ -0.01}$	623.21/795	<0.61
	0502220201	APM 08279+5255	165.759	+36.259	49.0	438	55.7	447	...	...	...	...	...	...
53	0556210401	SDSS J092829.86+504836.5	166.882	+45.200	13.1	376	12.9	542	621	1.46	2.1[c]	$0.52^{+0.90\ +0.35}_{-0.52\ -0.36}$	351.07/399	<1.14
54	0301340101	SDSS J083946.21+511203.0	167.648	+37.517	12.8	469	12.9	494	575	3.31	$1.92^{+0.29\ +0.09}_{-0.37\ -0.08}$	$2.41^{+1.48\ +0.77}_{-1.03\ -0.69}$	407.18/388	$1.54^{+1.07}_{-0.79}$
55	0402780701	SDSS J081040.29+481233.2	171.132	+32.731	13.0	407	13.7	553	471	4.54	2.1[c]	$0.00^{+0.52}_{-0.00} \pm 0.00$	400.35/416	<0.40
56	0553440101	SDSS J091709.55+463821.8	173.086	+43.961	9.3	332	9.6	499	638	1.47	2.1[c]	$0.08^{+0.95\ +0.48}_{-0.08\ -0.08}$	276.11/302	<0.88
57[d]	0406610501	HS 1111+4033	173.552	+65.922	14.6	334	14.7	419	730	1.45	2.1[c]	$0.99^{+1.13\ +0.42}_{-0.99\ -0.47}$	280.25/250	<1.68

Table 1
(Continued)

Sight line (1)	ObsID (2)	Target (3)	l (deg) (4)	b (deg) (5)	t_1^{exp} (ks) (6)	Ω_1 (arcmin^2) (7)	t_2^{exp} (ks) (8)	Ω_2 (arcmin^2) (9)	F/g R12 rate[a] (10)	N_H (10^{20} cm^{-2}) (11)	Halo T (10^6 K) (12)	Halo EM (10^{-3} cm^{-6} pc) (13)	χ^2/dof (14)	$S_{0.5-2.0}$[b] (15)
58	0503630201	CGCG 211−053	173.662	+56.052	14.6	321	15.1	481	792	1.11	2.1[c]	$0.44^{+0.78\ +0.39}_{-0.44\ -0.44}$	416.62/389	<1.01
59	0304203401	47 UMa	175.807	+63.353	8.4	359	8.3	381	763	1.19	$1.90^{+0.38\ +0.20}_{-0.25\ -0.07}$	$4.32^{+2.18\ +0.74}_{-1.99\ -1.13}$	231.97/223	$2.71^{+1.44}_{-1.43}$
60	0551630301	6C 1200+3416	176.503	+76.992	10.1	450	10.4	534	535	1.45	2.1[c]	$0.00^{+0.65}_{-0.00} \pm 0.00$	360.18/367	<0.50
61[d]	0406610101	HS 1036+4008	179.356	+59.942	10.0	374	10.2	452	806	1.65	$2.84^{+1.18\ +6.93}_{-0.68\ -0.44}$	$1.38^{+0.87\ +0.61}_{-0.78\ -0.52}$	277.13/263	$1.55^{+1.20}_{-1.05}$
62	0561580201	RE J1034+396	180.293	+59.048	32.4	315	35.4	380	811	1.31	$1.58^{+0.62}_{-0.55} \pm 0.05$	$1.22^{+3.90\ +0.65}_{-1.01\ -0.62}$	597.40/585	$0.46^{+1.49}_{-0.45}$
63	0504160101	Abell 122	181.277	−88.431	7.6	244	7.5	320	366	1.92	$1.99^{+1.04\ +0.13}_{-0.97\ -0.30}$	$1.49^{+4.77\ +0.33}_{-1.21\ -0.09}$	218.98/175	$1.03^{+3.31}_{-0.84}$
64	0400830301	6C 0905+3955	182.658	+42.566	42.3	402	42.9	491	527	1.74	$1.62^{+0.51\ +12.30}_{-0.37\ -0.05}$	$1.39^{+1.81\ +0.66}_{-0.85\ -0.96}$	470.94/594	$0.57^{+0.79}_{-0.53}$
65	0503601301	RXC J1022.0+3830	183.245	+56.906	11.3	212	11.0	315	819	1.56	$2.87^{+1.29\ +6.95}_{-0.64\ -0.21}$	$1.52^{+1.03\ +0.36}_{-0.94\ -0.52}$	308.27/237	$1.72^{+1.23}_{-1.22}$
66	0602290101	11 LMi	188.500	+47.781	43.8	411	45.1	493	689	1.22	$1.98^{+0.17\ +0.05}_{-0.31\ -0.11}$	$2.12^{+1.20\ +0.75}_{-0.66\ -0.49}$	552.19/595	$1.47^{+0.98}_{-0.57}$
67	0550960301	XBS J113148.7+311358	194.874	+72.188	21.6	369	21.1	470	559	2.05	2.1[c]	$0.00^{+0.67\ +0.48}_{-0.00\ -0.00}$	434.92/514	<0.63
68	0301651701	NGC 4169	197.309	+81.121	12.0	457	12.2	474	542	1.73	$1.76^{+0.26\ +0.06}_{-0.11\ -0.05}$	$4.38^{+0.89\ +1.14}_{-1.33\ -0.90}$	350.68/370	$2.26^{+0.74}_{-0.83}$
69	0602490101	DK Cet	197.430	−74.039	29.9	275	30.7	350	422	1.43	$3.09^{+1.17\ +0.41}_{-0.49\ -0.34}$	$0.96^{+0.54\ +0.31}_{-0.50\ -0.15}$	567.25/547	$1.16^{+0.75}_{-0.63}$
70[d]	0550270101	B2 1113+29	201.546	+69.008	6.7	306	6.7	320	642	1.24	2.1[c]	$2.70^{+1.74\ +0.58}_{-1.73\ -0.31}$	150.50/134	$2.06^{+1.41}_{-1.34}$
71	0502211201	W Comae	201.765	+83.269	6.1	362	6.5	436	521	2.04	$2.20^{+0.44\ +6.28}_{-0.32\ -0.05}$	$1.65^{+0.66\ +0.36}_{-0.46\ -1.02}$	528.40/472	$1.36^{+0.62}_{-0.92}$
	0502211401	W Comae	201.757	+83.270	8.5	295	8.8	436	...	...	...	...	...	...
72	0300630301	PKS 0237−23	209.821	−65.146	14.2	456	14.1	475	698	2.13	$1.60^{+1.53}_{-0.78} \pm 0.05$	$1.17^{+5.94\ +0.65}_{-1.13\ -0.67}$	381.23/392	<2.84
73	0556560101	Gl 436	210.550	+74.590	6.9	234	6.5	376	563	1.98	2.1[c]	$1.70^{+1.37\ +0.16}_{-1.39\ -0.57}$	204.12/166	$1.30^{+1.06}_{-1.15}$
74	0312190601	ESO 548−81	213.849	−50.846	10.8	312	11.3	392	427	2.29	2.1[c]	$0.74^{+1.17\ +0.39}_{-0.74\ -0.36}$	280.57/261	<1.51
75	0560191701	GRB 080913	223.044	−42.846	12.2	403	12.6	492	399	3.17	2.1[c]	$0.41^{+0.87\ +0.60}_{-0.41\ -0.41}$	315.71/382	<1.12
76	0555780401	*Chandra* Deep Field S	223.464	−54.373	5.5	320	5.9	467	466	0.702	2.1[c]	$0.01^{+0.23\ +0.41}_{-0.01\ -0.01}$	1749.48/1999	<0.36
	0604960201	*Chandra* Deep Field S	223.478	−54.372	72.1	388	77.3	468	...	...	...	...	...	...
	0555780201	*Chandra* Deep Field S	223.481	−54.365	73.1	379	78.3	467	...	...	...	...	...	...
	0555780101	*Chandra* Deep Field S	223.465	−54.365	34.2	378	34.7	466	...	...	...	...	...	...
77	0555781001	*Chandra* Deep Field S	223.645	−54.475	39.2	382	40.1	521	466	0.702	$2.11^{+0.15\ +0.17}_{-0.14\ -0.09}$	$0.95^{+0.10\ +0.20}_{-0.21\ -0.38}$	2448.33/3320	$0.73^{+0.17}_{-0.33}$
	0555782301	*Chandra* Deep Field S	223.645	−54.474	10.5	382	10.4	521	...	...	...	...	...	...
	0555780901	*Chandra* Deep Field S	223.631	−54.473	37.4	376	38.0	456	...	...	...	...	...	...
	0555780801	*Chandra* Deep Field S	223.616	−54.472	69.1	441	71.5	520	...	...	...	...	...	...
	0555780501	*Chandra* Deep Field S	223.620	−54.464	52.1	377	52.6	456	...	...	...	...	...	...
	0555780601	*Chandra* Deep Field S	223.632	−54.463	65.7	445	69.1	457	...	...	...	...	...	...
78	0301330401	F04103−2838	226.946	−45.906	19.4	405	19.4	563	417	2.73	2.1[c]	$0.22^{+0.66\ +0.56}_{-0.22\ -0.22}$	376.56/474	<0.83
79	0502690601	Abell 1413 offset	227.355	+76.300	35.1	323	35.0	472	647	2.18	$2.04^{+0.20\ +0.08}_{-0.34\ -0.14}$	$1.81^{+1.06\ +0.80}_{-0.41\ -0.55}$	444.32/579	$1.31^{+0.96}_{-0.50}$
80	0312190701	ESO 362−18	236.040	−32.583	10.9	395	10.8	485	573	1.75	$2.18^{+0.21\ +0.10}_{-0.26\ -0.08}$	$2.31^{+0.94\ +0.54}_{-0.73\ -0.47}$	316.53/319	$1.88^{+0.88}_{-0.71}$
81	0302500101	Fornax dSph	237.074	−65.638	22.1	326	23.7	556	597	3.01	$2.24^{+0.14\ +0.09}_{-0.13\ -0.07}$	$3.59^{+0.68\ +0.51}_{-0.66\ -0.63}$	381.18/450	$3.05^{+0.72}_{-0.77}$
82	0307001401	ESO 362−8	237.615	−34.679	7.7	405	8.1	501	666	2.63	$2.54^{+2.58\ +0.33}_{-0.75\ -0.09}$	$0.95^{+1.07\ +0.25}_{-0.89\ -0.26}$	273.97/287	$0.98^{+1.13}_{-0.96}$
83[d,e]	0505140201	NGC 1365	237.924	−54.594	32.5	369	34.2	464	576	1.34	$2.40^{+0.38\ +0.05}_{-0.19\ -0.10}$	$1.08^{+0.70\ +0.44}_{-0.28\ -0.07}$	1214.49/1162	$4.09^{+3.11}_{-1.09}$
	0505140501	NGC 1365	237.924	−54.593	40.0	304	43.5	402	...	...	...	...	...	...

Table 1
(Continued)

Sight line	ObsID	Target	l (deg)	b (deg)	$t_1^{\rm exp}$ (ks)	Ω_1 (arcmin^2)	$t_2^{\rm exp}$ (ks)	Ω_2 (arcmin^2)	F/g R12 rate[a]	$N_{\rm H}$ (10^{20} cm^{-2})	Halo T (10^6 K)	Halo EM (10^{-3} cm^{-6} pc)	χ^2/dof	$S_{0.5-2.0}$[b]
(1)	(2)	(3)	(4)	(5)	(6)	(7)	(8)	(9)	(10)	(11)	(12)	(13)	(14)	(15)
84	0555320301	1RXS J051723.3−352152	239.040	−33.596	6.6	298	6.6	452	615	4.13	2.1[c]	$1.77^{+1.46\ +0.65}_{-1.24\ -0.77}$	242.04/204	$1.36^{+1.22}_{-1.12}$
85	0301450301	Fairall 1116	244.612	−50.715	18.5	278	18.4	372	577	2.45	$2.25^{+0.79\ +7.15}_{-0.47\ -0.11}$	$1.38^{+0.80\ +0.49}_{-0.82\ -1.01}$	352.69/343	$1.18^{+0.81}_{-1.11}$
86	0501210701	APMUKS(BJ) B040410.	249.135	−47.779	21.2	396	21.3	479	454	1.24	$2.02^{+0.23\ +0.08}_{-0.34\ -0.11}$	$1.87^{+1.14\ +0.56}_{-0.69\ -0.48}$	432.59/502	$1.34^{+0.91}_{-0.60}$
87	0311792101	GRB 061121	249.356	+30.120	17.8	371	18.1	384	391	3.99	$1.73^{+0.35}_{-0.47} \pm 0.06$	$2.55^{+3.66\ +1.02}_{-1.33\ -0.86}$	447.17/405	$1.26^{+1.88}_{-0.78}$
88	0401130101	RX J0210.4−3929	254.996	−69.454	14.5	332	14.5	478	626	1.56	$2.68^{+0.27\ +0.19}_{-0.34\ -0.29}$	$2.22^{+0.55\ +0.68}_{-0.47\ -0.39}$	348.26/373	$2.38^{+0.94}_{-0.66}$
89	0303340101	RX J0136.9−3510	255.411	−77.394	38.6	429	40.3	518	540	2.08	$1.72^{+0.16}_{-0.11} \pm 0.05$	$2.53^{+0.81}_{-0.66} \pm 0.84$	551.69/592	$1.24^{+0.57}_{-0.52}$
90[d]	0501110201	RXC J0216.7−4749	269.794	−63.469	40.5	247	40.8	322	736	1.95	$2.87^{+0.65\ +0.45}_{-0.58\ -0.25}$	$1.20^{+0.62\ +0.36}_{-0.55\ -0.34}$	492.69/458	$1.36^{+0.82}_{-0.73}$
91[d]	0552410101	Beta Dor	271.714	−32.781	32.9	335	32.1	496	388	4.49	$2.27^{+0.53\ +0.38}_{-0.26\ -0.09}$	$3.24^{+1.69\ +0.67}_{-1.51\ -1.16}$	396.62/408	$2.81^{+1.58}_{-1.66}$
92	0551020701	Gl 86	275.884	−61.971	15.8	402	15.9	564	749	1.80	$2.28^{+0.38\ +0.30}_{-0.33\ -0.19}$	$1.76^{+0.89\ +0.12}_{-0.83\ -0.73}$	416.11/432	$1.54^{+0.79}_{-0.97}$
93	0550350101	RX J0134.2−4258	276.987	−71.915	20.7	368	22.1	450	667	1.67	$2.62^{+0.51\ +0.20}_{-0.43\ -0.24}$	$1.44^{+0.88\ +0.47}_{-0.63\ -0.25}$	456.94/536	$1.52^{+1.05}_{-0.72}$
94	0602920101	NGC 4561	277.794	+81.431	9.9	442	9.8	529	369	2.29	$1.71^{+0.26}_{-0.23} \pm 0.05$	$5.41^{+1.83\ +0.70}_{-1.59\ -1.02}$	349.90/373	$2.61^{+0.94}_{-0.91}$
95	0550950101	NGC 424	283.259	−78.254	91.0	299	91.0	377	576	1.56	$3.69^{+0.54\ +3.71}_{-0.32\ -0.35}$	$1.14^{+0.25\ +0.21}_{-0.26\ -0.49}$	757.91/594	$1.56^{+0.45}_{-0.77}$
96	0405090101	NGC 1313	283.360	−44.625	76.1	361	78.2	441	440	4.12	$2.28^{+0.11\ +0.09}_{-0.09\ -0.07}$	$4.05 \pm 0.64 \pm 0.61$	564.16/594	3.54 ± 0.77
97	0510181701	GRB 080411	292.093	−43.650	21.4	351	20.5	453	574	5.77	$2.22^{+0.12}_{-0.10} \pm 0.06$	$6.55^{+1.26\ +0.76}_{-1.00\ -0.74}$	461.98/482	$5.51^{+1.24}_{-1.05}$
98	0401930101	Q 0056−363	293.787	−80.881	39.8	370	39.5	381	547	1.87	$2.81^{+0.42\ +0.29}_{-0.31\ -0.22}$	$1.30^{+0.22\ +0.31}_{-0.40\ -0.25}$	642.35/590	$1.45^{+0.42}_{-0.52}$
99	0554500201	2MASX J01003469−4748303	298.568	−69.256	14.5	423	15.7	445	566	1.86	$2.11^{+0.31\ +0.09}_{-0.41\ -0.07}$	$2.22^{+0.93\ +0.56}_{-0.82\ -0.46}$	442.53/413	$1.71^{+0.83}_{-0.73}$
100[d]	0305860301	NGC 300	298.924	−79.434	35.1	163	35.1	212	563	3.97	$2.73^{+0.34\ +0.17}_{-0.37\ -0.13}$	$2.89^{+0.85\ +0.45}_{-0.84\ -0.47}$	308.05/289	3.15 ± 1.05
101	0301890101	ESO 113−10	299.461	−58.578	62.2	225	64.2	369	640	2.08	$1.77^{+0.15}_{-0.11} \pm 0.05$	$4.62^{+1.00\ +0.85}_{-0.83\ -0.84}$	599.94/580	$2.43^{+0.69}_{-0.62}$
102	0551021801	HD 4308	304.065	−51.445	10.0	331	10.0	557	769	1.92	$2.82^{+0.33\ +0.18}_{-0.26\ -0.11}$	$3.03^{+0.77\ +0.20}_{-0.80\ -0.45}$	332.60/321	$3.40^{+0.89}_{-1.03}$
103[f]	...	...	326.2	−58.0	...	...	...	...	...	...	$2.67^{+0.05}_{-0.04}$	3.04 ± 0.13	...	3.26 ± 0.14
103.1	0505381101	SZE SurF 11	324.176	−57.925	9.4	473	9.6	558	741	1.31	$2.33^{+0.19\ +0.10}_{-0.16\ -0.08}$	$3.51^{+0.85\ +0.52}_{-0.72\ -0.60}$	339.08/355	$3.18^{+0.91}_{-0.85}$
103.2	0505381901	SZE SurF 19	324.332	−58.336	9.7	339	9.4	558	732	1.23	$2.69^{+0.27\ +0.13}_{-0.32\ -0.29}$	$2.85^{+0.65\ +0.74}_{-0.58\ -0.39}$	287.14/320	$3.08^{+1.06}_{-0.75}$
103.3	0505383601	SZE SurF 36	324.580	−59.171	8.2	399	8.0	562	716	1.26	$2.62^{+0.26\ +0.11}_{-0.39\ -0.29}$	$3.02^{+1.37\ +0.96}_{-0.66\ -0.36}$	297.82/303	$3.20^{+1.77}_{-0.80}$
103.4	0505381001	SZE SurF 10	324.759	−57.704	12.5	471	12.2	552	730	1.37	$2.33^{+0.13\ +0.07}_{-0.11\ -0.06}$	$4.57^{+0.83\ +0.62}_{-0.61\ -0.56}$	423.04/405	$4.14^{+0.93}_{-0.75}$
103.5	0505381801	SZE SurF 18	324.919	−58.115	10.6	403	10.6	557	724	1.27	$2.65^{+0.22\ +0.11}_{-0.25\ -0.19}$	$3.07^{+0.66\ +0.57}_{-0.58\ -0.36}$	309.00/360	$3.27^{+0.93}_{-0.73}$
103.6	0505382701	SZE SurF 27	325.034	−58.540	10.1	349	11.1	568	719	1.22	$2.87^{+0.67\ +0.62}_{-0.38\ -0.15}$	$1.84^{+0.55\ +0.25}_{-0.66\ -0.56}$	365.59/371	$2.08^{+0.69}_{-0.98}$
103.7	0554560201	SZE SurF 2	325.220	−57.049	12.7	489	13.1	507	716	1.48	$2.75^{+0.22\ +0.14}_{-0.19\ -0.11}$	$2.95^{+0.48\ +0.34}_{-0.49\ -0.40}$	422.74/405	$3.24^{+0.64}_{-0.69}$
103.8	0505380901	SZE SurF 9	325.338	−57.477	5.8	342	5.7	498	718	1.42	$2.71^{+0.20\ +0.13}_{-0.21\ -0.11}$	$2.81^{+0.37\ +0.18}_{-0.40\ -0.36}$	514.68/520	$3.05^{+0.45}_{-0.58}$
	0505384801	SZE SurF 9	325.344	−57.475	9.6	339	9.3	569	...	...	...	...	...	...
103.9	0505382601	SZE SurF 26	325.620	−58.316	12.0	398	12.0	546	712	1.23	$2.59^{+0.19\ +0.10}_{-0.26\ -0.22}$	$3.19^{+1.08\ +0.72}_{-0.50\ -0.37}$	334.31/373	$3.35^{+1.37}_{-0.65}$
103.10	0554561001	SZE SurF 1	325.770	−56.815	10.1	479	10.1	494	702	1.48	$3.59^{+0.36\ +0.27}_{-0.33\ -0.22}$	$2.04^{+0.33\ +0.28}_{-0.36\ -0.27}$	381.94/373	$2.74^{+0.57}_{-0.60}$
103.11	0505383401	SZE SurF 34	325.777	−58.729	11.4	385	11.8	546	708	1.23	$2.82^{+0.20\ +0.13}_{-0.18\ -0.11}$	$3.34^{+0.60\ +0.42}_{-0.53\ -0.41}$	324.63/362	$3.73^{+0.82}_{-0.75}$
103.12	0505380801	SZE SurF 8	325.885	−57.246	8.8	344	8.8	571	706	1.42	$2.66^{+0.22\ +0.10}_{-0.31\ -0.23}$	$3.40^{+0.67\ +0.47}_{-0.54\ -0.39}$	263.12/296	$3.64^{+0.88}_{-0.71}$
103.13	0505384101	SZE SurF 41	325.906	−59.152	12.6	348	12.0	562	702	1.27	$2.40^{+0.20\ +0.09}_{-0.15\ -0.08}$	$4.13^{+0.69\ +0.27}_{-0.66\ -0.59}$	332.07/360	$3.92^{+0.70}_{-0.84}$
103.14	0505381601	SZE SurF 16	326.056	−57.659	7.0	329	9.0	479	706	1.33	$3.15^{+0.37\ +0.18}_{-0.28\ -0.12}$	$3.37^{+0.52}_{-0.75} \pm 0.36$	255.09/290	$4.11^{+0.77}_{-1.02}$

Table 1
(Continued)

Sight line (1)	ObsID (2)	Target (3)	l (deg) (4)	b (deg) (5)	$t_1^{\rm exp}$ (ks) (6)	Ω_1 (arcmin^2) (7)	$t_2^{\rm exp}$ (ks) (8)	Ω_2 (arcmin^2) (9)	F/g R12 rate[a] (10)	$N_{\rm H}$ (10^{20} cm^{-2}) (11)	Halo T (10^6 K) (12)	Halo EM (10^{-3} cm^{-6} pc) (13)	χ^2/dof (14)	$S_{0.5-2.0}$[b] (15)
103.15	0505382501	SZE SurF 25	326.192	−58.086	15.1	325	15.7	479	705	1.24	$2.36^{+0.26\ +0.10}_{-0.19\ -0.08}$	$3.08^{+0.99}_{-0.89} \pm 0.48$	331.23/416	$2.85^{+1.02}_{-0.94}$
103.16	0505383301	SZE SurF 33	326.360	−58.499	15.0	410	15.3	560	702	1.20	$2.73^{+0.24\ +0.16}_{-0.22\ -0.13}$	$2.40^{+0.51}_{-0.47} \pm 0.37$	443.26/432	$2.62^{+0.69}_{-0.65}$
103.17	0505384001	SZE SurF 40	326.495	−58.924	10.7	327	10.4	547	699	1.23	$2.86^{+0.21\ +0.12}_{-0.18\ -0.10}$	$3.49^{+0.70}_{-0.62} \pm 0.40$	297.66/336	$3.94^{+0.91}_{-0.83}$
103.18	0505381501	SZE SurF 15	326.611	−57.423	9.8	408	10.0	563	697	1.36	$2.73^{+0.23}_{-0.19} \pm 0.10$	$3.20^{+0.52\ +0.40}_{-0.44\ -0.32}$	329.69/335	$3.49^{+0.72}_{-0.60}$
103.19	0505382401	SZE SurF 24	326.752	−57.851	9.8	332	9.5	493	697	1.25	$2.35^{+0.29\ +0.10}_{-0.20\ -0.08}$	$3.44^{+1.06\ +0.55}_{-0.88\ -0.60}$	269.40/312	$3.17^{+1.10}_{-0.98}$
103.20	0505384901	SZE SurF 39	327.095	−58.724	6.5	390	6.7	553	694	1.19	$2.38^{+0.24\ +0.10}_{-0.17\ -0.07}$	$4.23^{+1.09}_{-1.06} \pm 0.63$	285.89/261	$3.95^{+1.18}_{-1.16}$
103.21	0505381401	SZE SurF 14	327.145	−57.183	10.9	338	11.0	562	688	1.38	$2.78^{+0.22\ +0.12}_{-0.20\ -0.10}$	$3.18^{+0.68\ +0.40}_{-0.57\ -0.38}$	338.38/348	$3.52^{+0.87}_{-0.75}$
103.22	0505382301	SZE SurF 23	327.302	−57.610	8.6	400	8.9	561	690	1.31	$2.77^{+0.42\ +0.13}_{-0.31\ -0.11}$	$2.41^{+0.82\ +0.29}_{-0.83\ -0.28}$	343.67/333	2.65 ± 0.96
103.23	0505383101	SZE SurF 31	327.480	−58.024	9.7	413	9.8	569	690	1.22	$2.75^{+0.23\ +0.13}_{-0.20\ -0.10}$	$3.12^{+0.63\ +0.41}_{-0.59\ -0.39}$	327.71/343	$3.42^{+0.82}_{-0.77}$
103.24	0505383801	SZE SurF 38	327.636	−58.450	11.2	345	11.1	488	689	1.16	$2.71^{+0.18}_{-0.15} \pm 0.10$	$3.91^{+0.62\ +0.44}_{-0.52\ -0.42}$	327.90/336	$4.25^{+0.83}_{-0.72}$
103.25	0505382201	SZE SurF 22	327.832	−57.366	13.1	316	13.1	541	682	1.33	$2.75^{+0.20\ +0.11}_{-0.19\ -0.10}$	$3.03 \pm 0.69^{+0.36}_{-0.32}$	396.87/399	$3.32^{+0.86}_{-0.83}$
103.26	0505383001	SZE SurF 30	328.020	−57.780	15.7	409	15.1	493	683	1.23	$2.94^{+0.10\ +0.13}_{-0.16\ -0.10}$	$3.45^{+0.56\ +0.44}_{-0.49\ -0.40}$	412.64/416	$3.98^{+0.83}_{-0.73}$
103.27	0505383701	SZE SurF 37	328.189	−58.206	9.5	327	9.8	552	684	1.16	$2.80^{+0.24\ +0.07}_{-0.20\ -0.10}$	$3.27^{+0.64\ +0.40}_{-0.55\ -0.26}$	289.81/312	$3.64^{+0.84}_{-0.67}$
104	0551150101	RR Tel	342.164	−32.242	28.2	362	32.2	515	430	4.18	$2.82 \pm 0.08^{+0.09}_{-0.08}$	$6.47^{+0.26\ +0.65}_{-0.35\ -0.63}$	603.24/586	$7.25^{+0.79}_{-0.81}$
105	0405380701	NGC 7590	348.256	−65.861	5.8	356	6.0	505	495	1.40	$3.41^{+1.00\ +8.33}_{-0.58\ -0.37}$	$2.19^{+1.04\ +1.59}_{-0.46\ -0.13}$	275.71/248	$2.83^{+2.46}_{-0.62}$
106	0504630101	Abell S1063	349.503	−59.948	12.0	272	13.1	355	506	1.24	$2.23^{+0.16\ +0.08}_{-0.12\ -0.06}$	$3.56^{+1.28\ +0.53}_{-1.21\ -0.51}$	300.21/309	$3.01^{+1.17}_{-1.11}$
107	0306080101	IC 5267	350.213	−61.785	36.9	379	37.8	480	477	1.21	$2.27^{+0.12\ +0.08}_{-0.11\ -0.07}$	$3.55^{+0.57\ +0.50}_{-0.48\ -0.49}$	501.50/589	$3.09^{+0.66}_{-0.60}$
108	0404520101	Abell 2811	357.613	−87.492	9.9	188	9.9	236	407	1.70	$2.31^{+1.06\ +0.22}_{-0.60\ -0.12}$	$1.91^{+1.70\ +0.67}_{-1.40\ -0.60}$	179.62/172	$1.71^{+1.64}_{-1.36}$
109	0402460201	Q 2130−431	357.988	−47.159	28.4	404	28.9	490	577	2.43	$2.40^{+0.16\ +0.20}_{-0.10\ -0.09}$	$4.28^{+0.71\ +0.73}_{-0.64\ -0.88}$	453.49/574	$4.07^{+0.97}_{-1.03}$
110	0553561101	2139.3−4235	358.305	−48.311	7.4	485	7.2	503	576	1.56	$3.11^{+0.74}_{-0.48} \pm 0.19$	$1.68^{+0.79\ +0.25}_{-0.71\ -0.20}$	289.13/330	$2.03^{+1.00}_{-0.89}$

Notes. Column 1 contains the sight line identification number; the sight lines are sorted in order of increasing l. Column 2 contains the *XMM-Newton* observation ID. Note that for some sight lines there is more than one *XMM-Newton* observation. Column 3 contains the name of the original target, in general taken from the FITS file header. If the target name was abbreviated or truncated, we attempted to get the full target name from SIMBAD. If the original target was a bright X-ray source, it was excised from the data, in order for us to measure the diffuse SXRB emission in the *XMM-Newton* field of view (see Section 2.2). Columns 4 and 5 contain the *XMM-Newton* pointing direction in Galactic coordinates. Column 6 contains the usable MOS1 exposure, after the exclusion of times affected by soft proton flaring and times of high solar wind proton flux. Column 7 contains the solid angle of the MOS1 detector from which the SXRB spectrum was extracted, after the exclusion of sources and unusable CCDs. Columns 8 and 9 contain the corresponding MOS2 data. Column 10 contains the R12 count rate used to fix the normalization of the foreground component of the spectral model (using data from Snowden et al. 2000; see Section 3.1.1). Column 11 contains the H I column density for the pointing direction (Kalberla et al. 2005). Columns 12 and 13 contain the best-fit halo temperature and emission measure (EM $= \int n_{\rm e}^2 dl$) for a 1T halo model. In each case, the first error is the statistical error (90% confidence interval), and the second is the estimated systematic error due to our assumed foreground and extragalactic models (see Section 3.2). Column 14 contains χ^2 and the number of degrees of freedom. Column 15 contains the intrinsic 0.5–2.0 keV surface brightness of the halo, calculated using the best-fit 1T model parameters. The error on the surface brightness is derived from the error on the emission measure (the statistical and systematic errors have been added in quadrature).

[a] 10^{-6} counts s^{-1} arcmin^{-2}.

[b] 10^{-12} erg cm^{-2} s^{-1} deg^{-2}.

[c] Temperature held fixed during fitting (see Section 3.1.2).

[d] For these sight lines, the exclusion regions used to excise bright and/or extended sources are different from those used in HS12 (see Section 2.2).

[e] This sight line was analyzed with a 2T model (see Section 3.1.2). The table contains the results for the cooler component. The parameters for the hotter component are: $T = (11.3^{+0.6\ +0.4}_{-0.4\ -0.3}) \times 10^6$ K, EM $= (2.8^{+0.4\ +0.6}_{-0.3\ -0.3}) \times 10^{-3}$ cm^{-6} pc.

[f] The temperature and emission measure for this sight line are the weighted means of the values for sight lines 103.1–103.27. The errors were calculated using the combined statistical and systematic errors from the individual sight lines' measurements. The surface brightness was calculated using the mean temperature and emission measure, with the error on the surface brightness derived from the error on the emission measure.

only the basic processing described above. One change we made was in our processing of observation 0305860301 (sight line 100). In HS12, we did not exclude the target galaxy, NGC 300, as a visual inspection of the X-ray images suggested it would not significantly contaminate the SXRB measurements. Here, however, we decided to err on the side of caution and excised the galaxy from the X-ray data before extracting the SXRB spectrum.

After our initial spectral extraction (described below), we found that on nine of our sight lines our spectral fitting (Section 3) yielded halo temperatures of $\sim 10 \times 10^6$ K. Such temperatures are much higher than those that are typically observed in the halo ($T \sim (2\text{–}3) \times 10^6$ K; Smith et al. 2007b; Galeazzi et al. 2007; Gupta et al. 2009; Lei et al. 2009; Yoshino et al. 2009; HSKJM). For these sight lines, we re-examined the X-ray images. In particular, we used *XMM*-ESAS tools to create adaptively smoothed, particle-background-subtracted, flat-fielded images in the 0.4–1.3 keV band (the upper energy limit was chosen to avoid the Al instrumental line at 1.49 keV). These images revealed regions of diffuse emission that had not been adequately excised by the original exclusion regions. We therefore excluded these additional regions and re-extracted the spectra. The affected observations are indicated by a "d" in Column 1 of Table 1. After this change, our spectral analysis yields halo temperatures of $\sim(2\text{–}3) \times 10^6$ K on all but one of these nine sight lines. Note that the additional sources we have removed appear not to have contaminated the $\sim(2\text{–}3) \times 10^6$ K halo emission. Therefore, the measurements of this emission from the other sight lines (for which we used the source exclusion regions straight from HS10 and HS12) should be reliable (Section 5.3).

In addition to removing bright sources and regions of extended emission, we automatically identified and removed sources within each field with 0.5–2.0 keV fluxes $F_{\rm X}^{0.5-2.0} \geqslant 1 \times 10^{-14}$ erg cm^{-2} s^{-1} (cf. 5×10^{-14} erg cm^{-2} s^{-1} in HS12). In general, we obtained the source locations and fluxes from the 2XMMi DR3 data release of the Second *XMM-Newton* Serendipitous Source Catalog[5] (Watson et al. 2009). For this flux threshold, the catalog is >90% complete (Watson et al. 2009). Note that although we only used MOS data in our spectral analysis, the Serendipitous Source Catalog also made use of data from the pn camera. We excluded the sources identified from the catalog using circles of radius 50″. Such regions enclose ∼90% of each source's flux. In Section 5.3, we discuss potential contamination from the photons that spill out of these source exclusion regions.

Approximately 10% of our observations were not included in the Serendipitous Source Catalog. For these observations, we ran the source detection ourselves, using the standard *XMM-Newton* `edetect_chain` script. Following Watson et al. (2009), we carried out the source detection simultaneously in five bands (0.2–0.5, 0.5–1.0, 1.0–2.0, 2.0–4.5, and 4.5–12.0 keV) using data from the two MOS cameras. For exposures exceeding 5 ks (the minimum exposure for inclusion in the HS12 catalog), the MOS cameras can detect sources with $F_{\rm X}^{0.5-2.0} \geqslant 1 \times 10^{-14}$ erg cm^{-2} s^{-1} (Watson et al. 2001, Figure 3). Again, we excluded the sources exceeding the flux threshold using circles of radius 50″.

For each exposure of each observation, we used the `mos-spectra` script to extract an SXRB spectrum from the full *XMM-Newton* field of view, minus any excluded sources, and minus any unusable CCDs (e.g., those in window mode or those exhibiting the anomalous state described by Kuntz & Snowden 2008). The solid angles of the MOS1 and MOS2 detectors from which the spectra were extracted are shown in Columns 7 and 9 of Table 1, respectively. We grouped the SXRB spectra such that each spectral bin contained at least 25 counts. The `mos-spectra` script also produced the required response files for each spectrum, namely a redistribution matrix file and an ancillary response file, using the SAS `rmfgen` and `arfgen` tasks, respectively.

For each SXRB spectrum, we calculated a corresponding quiescent particle background (QPB) spectrum using the *XMM*-ESAS `mos_back` program. The QPB spectra were constructed from a database of MOS data obtained with the filter wheel in the closed position, scaled to our observations using data from the unexposed corner pixels that lie outside the MOS field of view (Kuntz & Snowden 2008). Before we carried out our spectral analysis, we subtracted from each SXRB spectrum the corresponding QPB spectrum.

3. SPECTRAL ANALYSIS METHOD

3.1. Model Description

We used XSPEC[6] version 12.7.0k to carry out the spectral fitting. Our spectral model consisted of components to model the foreground emission from SWCX (and possibly also from the Local Bubble), the Galactic halo emission (which is the component that we are interested in here), and the extragalactic background of unresolved AGNs. In addition, the model included components to model the parts of the instrumental particle background that are not removed by the QPB subtraction. Our model, described below, is the same as that used in HSKJM, apart from the component used to model the extragalactic background and, for one sight line, the halo emission model.

3.1.1. Foreground Emission

We used a single-temperature ($1T$) Raymond & Smith (1977 and updates) model with $T = 1.2 \times 10^6$ K (Snowden et al. 2000) to model the foreground emission. For each sight line, we fixed the normalization of this component based on the foreground R12 count rates for the five nearest shadows in the Snowden et al. (2000) *ROSAT* shadow catalog (see HSKJM for details).

3.1.2. Halo Emission

We typically used a $1T$ Raymond & Smith (1977 and updates) model to model the Galactic halo emission, assuming that the halo plasma is in collisional ionization equilibrium, and assuming Anders & Grevesse (1989) solar abundances. Although the true halo emission is likely from plasma at a range of temperatures (Yao & Wang 2007; Shelton et al. 2007; Lei et al. 2009; Yao et al. 2009), a $1T$ model is generally adequate to characterize the X-ray emission in the *XMM-Newton* band. We used a Raymond & Smith model in order to match the code used to calculate X-ray emission from hydrodynamical models of the halo (HSKJM; D. B. Henley et al., in preparation). In general, the temperature and emission measure of this component were free parameters in the fitting. In some cases, typically when the halo emission was faint, XSPEC's `error` command was unable to determine the statistical error on the halo temperature. In a few additional cases, the best-fit temperature was $>5 \times 10^6$ K,

[5] http://xmmssc-www.star.le.ac.uk/Catalogue/2XMMi-DR3/

[6] http://heasarc.gsfc.nasa.gov/docs/xanadu/xspec/

but very poorly constrained. In such cases, we fixed the halo temperature at 2.1×10^6 K, and redid the fit. This temperature was chosen as it was the median halo temperature resulting from our preliminary analysis of our data set.

As noted in Section 2.2, for nine of our sight lines, we initially found that fitting with the above $1T$ model yielded a temperature that was unusually high and that was well constrained, such that T was significantly greater than 4×10^6 K. In general, these high temperatures appeared to be due to excess emission around ~1 keV, although on about a third of the sight lines the excess was only slight. As described in Section 2.2, we re-examined these sight lines, using newly created adaptively smoothed, QPB-subtracted images. We identified and removed additional regions of diffuse emission that could have been contaminating the spectra. After this modification, only one sight line (number 83) yielded an unusually high halo temperature ($T \sim 10 \times 10^6$ K), although on some other sight lines, there is still some excess emission around ~1 keV apparent in the spectra. For sight line 83 alone, we used a two-temperature ($2T$) model to model the non-foreground, non-extragalactic-background emission: one component to model the excess emission around ~1 keV, and one to model the ~(2–3) $\times 10^6$ K halo emission. In the plots and tables that follow, we use the results for the ~(2–3) $\times 10^6$ K halo component for this sight line.

3.1.3. Extragalactic Background

HSKJM followed HS10 and modeled the extragalactic background as a power law with a photon index $\Gamma = 1.46$ and a normalization at 1 keV of 10.5 photons cm^{-2} s^{-1} sr^{-1} keV^{-1} (Chen et al. 1997). However, there is evidence that the extragalactic background steepens below 1 keV (Roberts & Warwick 2001). Furthermore, below 2 keV, the summed spectrum of the faint sources that compose the extragalactic background has $\Gamma = 1.96$ (Hasinger et al. 1993), compared with $\Gamma \approx 1.4$ for the 3–10 keV extragalactic background (Marshall et al. 1980). We therefore adopted a different model for the extragalactic background here. Specifically, we used the double broken power-law model from Smith et al. (2007b). The first component has a break energy of $E_b = 1.2$ keV, photon indices below and above the break of $\Gamma_1 = 1.54$ and $\Gamma_2 = 1.4$, respectively, and a normalization of 5.70 photons cm^{-2} s^{-1} sr^{-1} keV^{-1}. The second component has $E_b = 1.2$ keV, with $\Gamma_1 = 1.96$, $\Gamma_2 = 1.4$, and a normalization of 4.90 photons cm^{-2} s^{-1} sr^{-1} keV^{-1}.

We rescaled this model so that its 0.5–2.0 keV surface brightness would be equal to the integrated surface brightness expected from sources with $F_X^{0.5-2.0} < 1 \times 10^{-14}$ erg cm^{-2} s^{-1} (this is the flux threshold for the automated source removal; see Section 2.2). Hickox & Markevitch (2006) measured the 0.5–2.0 keV surface brightness of the unresolved extragalactic background to be $(1.57 \pm 0.41) \times 10^{-12}$ erg cm^{-2} s^{-1} deg^{-2}, after removing sources with $F_X^{0.5-2.0} \geqslant 2.5 \times 10^{-17}$ erg cm^{-2} s^{-1}. This is the average of the surface brightness measurements for the Chandra Deep Field North (CDF-N) from their Table 3, attenuated by an absorbing column of 1.5×10^{20} cm^{-2} (the value for the CDF-N; Hickox & Markevitch 2006), with the error rescaled to a 90% confidence interval. The 0.5–2.0 keV surface brightness of sources with $F_X^{0.5-2.0} = 2.5 \times 10^{-17}$ to 1×10^{-14} erg cm^{-2} s^{-1}, meanwhile, is expected to be 2.97×10^{-12} erg cm^{-2} s^{-1} deg^{-2} (using the source flux distribution from Moretti et al. 2003). Hence, we rescaled the Smith et al. (2007b) extragalactic model such that its observed 0.5–2.0 keV surface brightness (assuming an absorbing column of 1.5×10^{20} cm^{-2}, the value for the CDF-N; Hickox & Markevitch 2006) is 4.54×10^{-12} erg cm^{-2} s^{-1} deg^{-2}. This corresponds to normalizations of 3.59 and 3.09 photons cm^{-2} s^{-1} sr^{-1} keV^{-1}, respectively, for the two components. In Section 3.2, we describe how we estimated the systematic errors associated with our fixing the normalizations of the extragalactic model components at these nominal values.

The halo and extragalactic components were both subject to absorption. For this purpose we used the XSPEC `phabs` model (Bałucińska-Church & McCammon 1992, with an updated He cross-section from Yan et al. 1998). For each sight line, the absorbing column density was fixed at the H I column density from the Leiden–Argentine–Bonn Survey (Kalberla et al. 2005; values were obtained using the HEAsoft `nh` tool).

3.1.4. Particle Background

In addition to the above-described SXRB components, our model included components to model any residual soft proton contamination that remains after the data cleaning described in Section 2.2, and to model the instrumental Al and Si fluorescence lines at 1.49 and 1.74 keV, respectively. For the former, we used a power-law model that was not folded through the instrumental response (Snowden & Kuntz 2011), while for the latter we used two Gaussians. The parameters for the soft proton power laws and for the instrumental lines were free parameters in the fits, and were independent for each MOS exposure. See HSKJM for more details.

For each sight line, we fitted the above-described model to the 0.4–5.0 keV MOS1 and MOS2 spectra simultaneously. In most cases, this involved fitting to the spectra from a single *XMM-Newton* observation. However, for some sight lines we fitted the model to the spectra from multiple observations (see Section 2.1).

3.2. Systematic Errors

In our spectral analysis, we fixed both the normalization of the foreground component (estimated using *ROSAT* shadowing data from Snowden et al. 2000) and the normalization of the extragalactic background (using the surface brightness expected for this background given the source removal flux threshold; Moretti et al. 2003; Hickox & Markevitch 2006). We fixed the normalization of the foreground component in order to avoid having a degeneracy at low energies between the foreground and halo emission, and we fixed the normalization of the extragalactic background in order to avoid having a degeneracy at high energies between this component and the power law used to model the residual soft proton contamination. Because fixing these model parameters may bias our best-fit halo parameters, introducing systematic errors to our results, here we estimate the magnitudes of these systematic errors, using essentially the same method as described in HSKJM (although note that HSKJM did not take into account cosmic variance; see below).

To estimate the systematic errors due to our fixing the foreground normalization, we reanalyzed each sight line with a foreground normalization corresponding to an R12 count rate of 610 counts s^{-1} arcmin^{-2} (this is the median of the values in Column 10 of Table 1). We then used the median differences between the original halo parameters and these new halo parameters to estimate the systematic errors due to our fixing the foreground normalization, yielding $\pm 0.046 \times 10^6$ K and ± 0.027 dex for the halo temperature and emission measure, respectively. We applied these systematic errors to all sight lines.

Our estimate of the systematic errors due to our fixing the extragalactic normalization is based on three uncertainties: (1) the uncertainty on the summed surface brightness of sources with $F_X^{0.5-2.0} = 2.5 \times 10^{-17}$ to 1×10^{-14} erg cm^{-2} s^{-1} in a given field, due to Poissonian field-to-field variation of the numbers of such sources (estimable from the Moretti et al. 2003 source flux distribution); (2) the uncertainty on the measured surface brightness of the unresolved extragalactic background after removing sources with $F_X^{0.5-2.0} \geqslant 2.5 \times 10^{-17}$ erg cm^{-2} s^{-1} (Hickox & Markevitch 2006); and (3) field-to-field variations in the number of sources composing the extragalactic background due to clustering of said sources (cosmic variance). For uncertainty (1), we used a Monte Carlo simulation to estimate the field-to-field variation in the summed surface brightness of sources with $F_X^{0.5-2.0} = 2.5 \times 10^{-17}$ to 1×10^{-14} erg cm^{-2} s^{-1}, due to Poissonian fluctuations in the number of said sources. We estimated this variation to be $\pm 0.22 \times 10^{-12}$ erg cm^{-2} s^{-1} deg^{-2} (90% confidence interval) for *XMM-Newton*-sized fields. For uncertainty (2), we used the measurement error from Hickox & Markevitch (2006) quoted in Section 3.1.3: $\pm 0.41 \times 10^{-12}$ erg cm^{-2} s^{-1} deg^{-2} (90% confidence interval).

For uncertainty (3), we followed Hickox & Markevitch (2006), and used Equation (45.6) from Peebles (1980) to calculate the variance in the number of sources due to source clustering, $\sigma^2_{\rm clus}$, for a field of solid angle Ω:

$$\frac{\sigma^2_{\rm clus}}{N^2} = \int\int w(\theta_{12}) d\Omega_1 d\Omega_2, \quad (1)$$

where N is the expectation value of the number of sources in the field, and $w(\theta_{12})$ is the two-point angular correlation coefficient. Note that this variance is in addition to that due to Poissonian fluctuations. Vikhlinin & Forman (1995) found that the clustering of extragalactic X-ray sources could be described by $w(\theta_{12}) = (\theta_{12}/\theta_0)^{1-\gamma}$, with $\theta_0 = 4''$ and $\gamma \approx 1.8$. Substituting this into Equation (1) and integrating over a field of radius $15'$ (the approximate size of the *XMM-Newton* field of view), the expected field-to-field variation in the number of extragalactic sources due to clustering is $\pm 14\%$ (1σ). Assuming that this clustering is independent of source flux, this variation corresponds to a field-to-field variation in the surface brightness of $\pm 1.03 \times 10^{-12}$ erg cm^{-2} s^{-1} deg^{-2} (90% confidence interval).

Combining uncertainties (1)–(3) in quadrature, we estimate that for *XMM-Newton*-sized fields, the 0.5–2.0 keV surface brightness of the extragalactic background will typically lie in the range (3.41–5.66) $\times 10^{-12}$ erg cm^{-2} s^{-1} deg^{-2} (90% confidence interval). We therefore reanalyzed each sight line twice, with the extragalactic model rescaled to give 0.5–2.0 keV surface brightnesses of 3.41×10^{-12} and 5.66×10^{-12} erg cm^{-2} s^{-1} deg^{-2}, respectively (our original extragalactic model had a surface brightness of 4.54×10^{-12} erg cm^{-2} s^{-1} deg^{-2}). During each fit, the surface brightness of the extragalactic model was fixed at the specified value. We used the differences between these new results and the original results to estimate the systematic errors (90% confidence intervals) due to our fixing the extragalactic normalization. Note that when we adjust the normalization of the extragalactic model from its original value, the best-fit soft proton model changes in response, and the changes in both the components alter the best-fit halo model. Therefore, this estimated systematic error due to our fixing the extragalactic normalization also takes into account the uncertainty in the soft proton contamination.

In summary, for each sight line and for each halo model parameter, we estimated the systematic error due to our fixing the foreground normalization and that due to our fixing the extragalactic normalization. We added these errors in quadrature to yield our final estimate of the systematic error.

4. SPECTRAL ANALYSIS RESULTS

Our spectral modeling inputs and results are shown in Columns 10–15 of Table 1. For each sight line with multiple *XMM-Newton* observations, the fit results are shown against the first listed observation; Columns 10–15 are empty for that sight line's other observations. Column 10 contains the foreground R12 count rate used to fix the normalization of the foreground component (Section 3.1.1). Column 11 contains the absorbing H I column density used to attenuate the halo and extragalactic components. Column 12 contains the best-fit halo temperature, along with the statistical error (90% confidence interval for one interesting parameter; Lampton et al. 1976) and the systematic error (Section 3.2). Similarly, Column 13 contains the best-fit halo emission measure. As noted in Section 2.1, the results for sight line 103 were obtained by averaging the results for sight lines 103.1–103.27. Column 14 contains χ^2 and the number of degrees of freedom. Column 15 contains the intrinsic 0.5–2.0 keV surface brightness of the halo, $S_{0.5-2.0}$. The *XMM-Newton* spectra and best-fit models for two typical observations are shown in Figure 1.

We noted in Sections 2.2 and 3.1.2 that our $1T$ halo model yielded an unusually high halo temperature for sight line 83 (Figure 2(a)). This high temperature appears to be due to excess emission around ~1 keV—see Figure 2(b), in which the halo temperature was fixed at 2.5×10^6 K. For this sight line, we used a $2T$ model to model the non-foreground, non-extragalactic-background emission (Figure 2(c)). The origin of the excess emission around ~1 keV (which is also apparent on a small number of other sight lines) is uncertain. It is unlikely to be due to SWCX emission from Fe and Ne. This is because all of our *XMM-Newton* observations were taken during solar minimum toward high ecliptic latitudes (see Section 2.1), and so our observations mostly sample the low-ionization slow solar wind in which high Fe and Ne ions are not expected (Yoshino et al. 2009). It is also unlikely to be due to faint sources below our source removal flux threshold ($F_X^{0.5-2.0} < 1 \times 10^{-14}$ erg cm^{-2} s^{-1}). Gupta & Galeazzi (2009) examined the stacked spectrum of sources with $F_X^{0.5-2.0} < 1 \times 10^{-14}$ erg cm^{-2} s^{-1}, and found excess emission around 1 keV. This excess, which they attributed to Milky Way stars, could be fitted with a thermal plasma model with $T = 10.7 \times 10^6$ K. However, the 0.5–2.0 keV surface brightness of this component is only 0.065×10^{-12} erg cm^{-2} s^{-1} deg^{-2}, which is a factor of ~50 less than the surface brightness of the hotter component measured on sight line 83. This excess emission may be due to extragalactic diffuse emission lying in the field of view, although we have attempted to minimize such emission. However, the presence of such emission on sight line 83 (and potentially on other sight lines) appears not to be contaminating our measurements of the ~(2–3) $\times 10^6$ K halo plasma (see Section 5.3).

The halo emission measures and intrinsic surface brightnesses are plotted against the halo temperatures in Figure 3, with marginal histograms showing the distributions of these quantities. We define halo emission as having been detected on a sight line if the combined statistical and systematic confidence interval on the emission measure does not include zero. Overall,

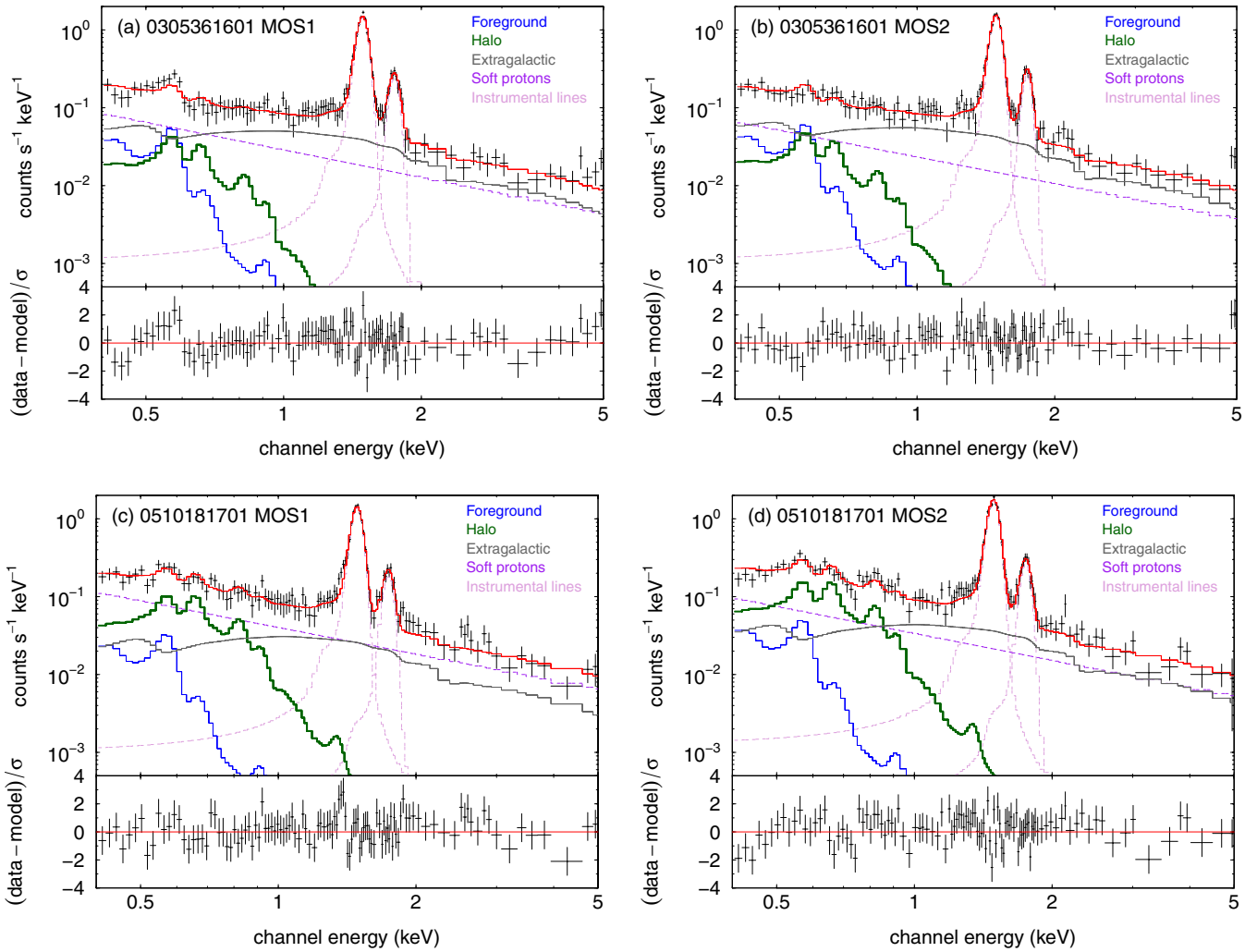

Figure 1. *XMM-Newton* MOS1 (left) and MOS2 (right) spectra and best-fit 1T halo models for two example observations: 0305361601 (sight line 11; top row) and 0510181701 (sight line 97; bottom row). The best-fit model is shown in red, and the individual model components are plotted in different colors (see key). Note that the two components of the extragalactic background have been summed. The components that model parts of the particle background (the soft protons and the instrumental lines) are plotted with dashed lines. For the fitting, the spectra were grouped such that there were at least 25 counts per bin, prior to subtraction of the QPB. For plotting purposes only, we have further grouped the spectra so that each bin has a signal-to-noise ratio of at least 3.

(A color version of this figure is available in the online journal.)

we detected emission from plasma with $T \sim (2\text{–}3) \times 10^6$ K on 87 of our 110 sight lines (79%). For the vast majority of the sight lines with such detections (83/87), we did not have to fix the halo temperature at 2.1×10^6 K. For sight lines with detections, the temperature of the halo is typically $(2.0\text{–}2.6) \times 10^6$ K (Table 2, row 1). The corresponding emission measures span an order of magnitude, lying mostly in the range $\sim(0.8\text{–}5) \times 10^{-3}$ cm^{-6} pc, with lower and upper quartiles of 1.4×10^{-3} and 3.0×10^{-3} cm^{-6} pc, respectively (Table 2, row 1). The intrinsic 0.5–2.0 keV surface brightnesses lie mostly in the range $\sim(0.6\text{–}4) \times 10^{-12}$ erg cm^{-2} s^{-1} deg^{-2}, with lower and upper quartiles of 1.1×10^{-12} and 2.3×10^{-12} erg cm^{-2} s^{-1} deg^{-2}, respectively (Table 2, row 1).

For 22 of the 23 sight lines on which we did not detect halo emission, we had to fix the halo temperature at 2.1×10^6 K. For the other sight line (number 72), we were able to constrain the halo temperature because the statistical error on the emission measure alone does not include zero (although the combined statistical and systematic error does include zero). Among the sight lines that yielded non-detections, the lower and upper quartiles of the upper limits on the emission measures are 0.8×10^{-3} and 1.4×10^{-3} cm^{-6} pc, respectively, while the lower and upper quartiles of the upper limits on the intrinsic 0.5–2.0 keV surface brightnesses are 0.6×10^{-12} and 1.1×10^{-12} erg cm^{-2} s^{-1} deg^{-2}, respectively (Table 2, row 2).

Figure 4 shows maps of the measured halo temperatures and emission measures. From a visual inspection of Figures 4(a) and (c), it appears that the halo temperature is in general rather uniform. Figures 4(b) and (d), meanwhile, show that there is considerable variation in the emission measure of the halo plasma. In the northern hemisphere, no clear trends are apparent from Figure 4(b) (although see Section 4.1). From Figure 4(d), it appears that the halo emission measure in the south tends to increase from the outer Galaxy ($l = 180°$) to the inner Galaxy ($l = 0°$), a trend which we will confirm in the following section.

4.1. Variation with Galactic Longitude and Latitude

Table 3 shows the correlation coefficients (Kendall's τ; e.g., Press et al. 1992) for the halo temperature and emission measure against the absolute values of Galactic longitude and latitude, $|l|$

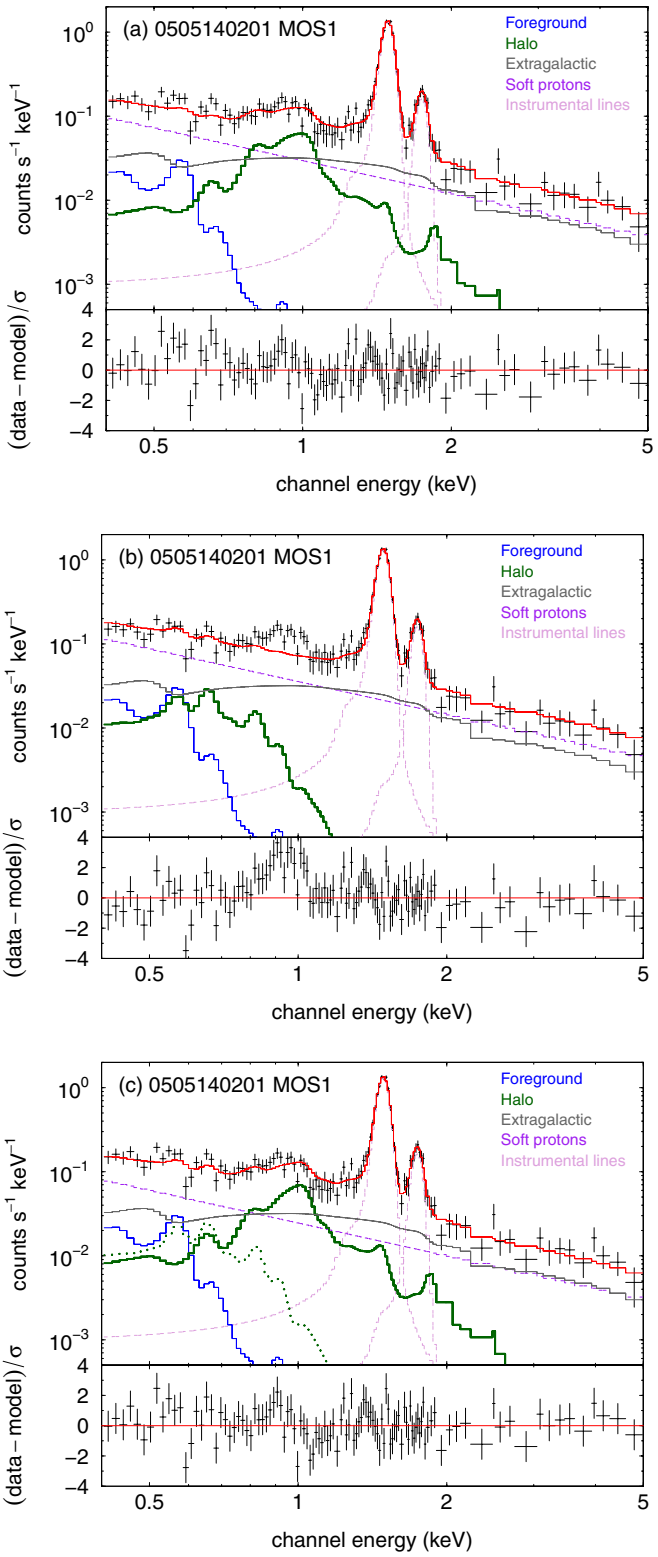

Figure 2. *XMM-Newton* MOS1 spectra and best-fit models for observation 0505140201 (from sight line 83). The initial fitting on this sight line with a $1T$ halo model yielded an unusually high halo temperature ($T \sim 10 \times 10^6$ K; panel (a)). This high temperature is due to excess emission around 1 keV; this excess emission is apparent when we fix the halo temperature at 2.5×10^6 K (panel (b)). For this sight line we used a $2T$ model to model the non-foreground, non-extragalactic-background emission (panel (c)). The green dotted line shows the emission from the ∼(2–3) $\times 10^6$ K halo, while the green solid line shows the emission from the hotter component, of unknown origin. The spectra are grouped as in Figure 1.

(A color version of this figure is available in the online journal.)

and $|b|$, respectively. We define the absolute value of longitude as

$$|l| = \begin{cases} l & \text{if } l < 180^\circ; \\ 360^\circ - l & \text{otherwise;} \end{cases} \quad (2)$$

i.e., in both the western and eastern Galactic hemispheres, $|l|$ increases from 0° toward the Galactic center to 180° toward the Galactic anticenter. When calculating the correlation coefficients for the halo temperature against $|l|$ or $|b|$, we omitted the sight lines for which we had to fix the temperature at 2.1×10^6 K. When calculating the correlation coefficients for the halo emission measure against $|l|$ or $|b|$, we did not omit such sight lines. We used the best-fit emission measures for all sight lines, whether or not a given sight line yielded a detection or an upper limit. Note from Figure 4 that in each hemisphere there are one or two sight lines that are isolated from the majority of the sight lines in that hemisphere: in the north there is a single sight line at $(l, b) \approx (250^\circ, +30^\circ)$, and in the south there is a pair of sight lines near $(l, b) = (90^\circ, -35^\circ)$. These sight lines were excluded from the correlation coefficient calculations.

In only two cases is the correlation statistically significant at the 5% level. The halo emission measure is positively correlated with $|b|$ in the northern hemisphere (i.e., the emission measure tends to increase from low latitudes to the pole; see Figure 5(a)). There is no correlation between emission measure and $|b|$ in the southern hemisphere (see Figure 5(b)). However, the emission measure is negatively correlated with $|l|$ in the southern hemisphere (i.e., the emission measure tends to increase from the outer Galaxy to the inner Galaxy, as noted in the previous section; see Figure 5(d)).

The correlation between emission measure and $|b|$ in the north (Figure 5(a)) may in part be due to the fact that there are more upper limits below 60° than above 60°. For such sight lines, we used the best-fit emission measures (which are zero for several sight lines). If, instead, we use the upper limits on the emission measures in the correlation coefficient calculation, the correlation is still significant, albeit with a higher p-value ($\tau = 0.17$, p-value $= 0.044$). However, if we omit the sight lines that yield upper limits, the correlation is not statistically significant ($\tau = 0.11$, p-value $= 0.27$).

In contrast, the correlation between emission measure and $|l|$ in the south (Figure 5(d)) remains if we use the upper limits for sight lines with non-detections ($\tau = -0.34$, p-value $= 1.6 \times 10^{-3}$) or if we omit the non-detections altogether ($\tau = -0.36$, p-value $= 1.7 \times 10^{-3}$). The exclusion of the region around the Sco-Cen superbubble may limit our ability to detect a similar trend in the northern hemisphere, as observations with smaller values of $|l|$ are excluded from our data set (see Figure 5(c)). However, it should be noted that if we exclude a similar region toward the inner Galaxy in the southern hemisphere ($|l| \leqslant 50^\circ$), the correlation between emission measure and $|l|$ remains significant ($\tau = -0.46$, p-value $= 1.5 \times 10^{-5}$). This suggests that rather than the lack of a significant observed correlation being an artifact of the exclusion of the region around the Sco-Cen superbubble, the emission measure does not vary systematically with $|l|$ in the northern hemisphere as it does in the south.

4.2. Differences between the Galactic Hemispheres

In the previous subsection, we found that the two Galactic hemispheres are different when it comes to correlations of the halo emission measure with $|l|$ and $|b|$. In this subsection, we describe evidence of other differences between the hemispheres.

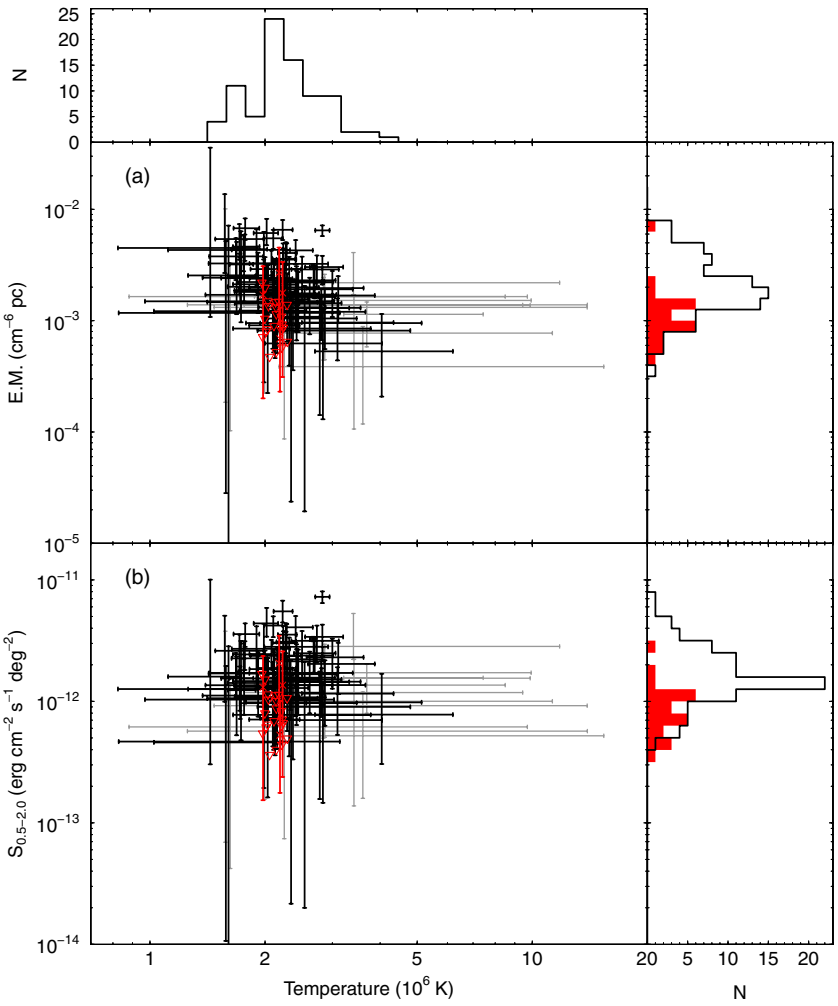

Figure 3. (a) Halo emission measure and (b) intrinsic 0.5–2.0 keV halo surface brightness against halo temperature, from our spectral modeling. Black: the temperature was free to vary, and is well constrained. Gray: the temperature was free to vary, but is poorly constrained (combined statistical and systematic confidence interval spans more than 4×10^6 K). Red: the temperature was fixed at $T = 2.1 \times 10^6$ K (see Section 3.1.2). The red triangles indicate upper limits on the emission measures and surface brightnesses. Note that to avoid clutter, the red data points have been randomly displaced by small amounts in the horizontal direction from $T = 2.1 \times 10^6$ K. Top panel: histogram of halo temperatures. The sight lines on which the temperature was fixed have been omitted. Side panels: histograms of halo emission measures (upper panel) and intrinsic surface brightnesses (lower panel). Black: detections; red: upper limits.

(A color version of this figure is available in the online journal.)

Table 2
Medians and Quartiles of the Halo Temperature, Emission Measure, and Surface Brightness

Row	Data Subset	Temperature (10^6 K)				Emission Measure (10^{-3} cm^{-6} pc)				$S_{0.5-2.0}$[a]			
		N	LQ	Med	UQ	N	LQ	Med	UQ	N	LQ	Med	UQ
1	Full data set—detections[b]	83	2.01	2.22	2.64	87	1.38	1.91	3.04	87	1.14	1.54	2.34
2	Full data set—non-detections (upper limits)	...	...	...	...	23	0.81	1.04	1.43	23	0.62	0.80	1.09
3	Northern Galactic hemisphere[c]	45	1.76	2.13	2.37	66	0.52	1.41	2.12	66	0.44	1.07	1.56
4	Southern Galactic hemisphere[c]	38	2.13	2.30	2.72	44	1.27	2.05	3.32	44	1.18	1.71	3.06
5	Southern Galactic hemisphere ($\|l\| > 50°$)[c,d]	27	2.11	2.28	2.71	33	1.14	1.49	2.53	33	1.03	1.45	2.43

Notes. For each quantity, we tabulate the number of sight lines (N), the lower quartile (LQ), the median (Med), and the upper quartile (UQ). The results are taken from Columns 12, 13, and 15 of Table 1.

[a] Intrinsic 0.5–2.0 keV surface brightness in 10^{-12} erg cm^{-2} s^{-1} deg^{-2}.

[b] When calculating the quartiles of the temperatures, we exclude sight lines for which the temperature is fixed at 2.1×10^6 K.

[c] When calculating the quartiles of the temperatures, we exclude non-detections and sight lines for which the temperature is fixed at 2.1×10^6 K. When calculating the quartiles of the emission measures, we use the best-fit emission measures from Table 1 for all sight lines, including those that yield non-detections (and similarly for the surface brightnesses).

[d] See Equation (2) for the definition of $|l|$.

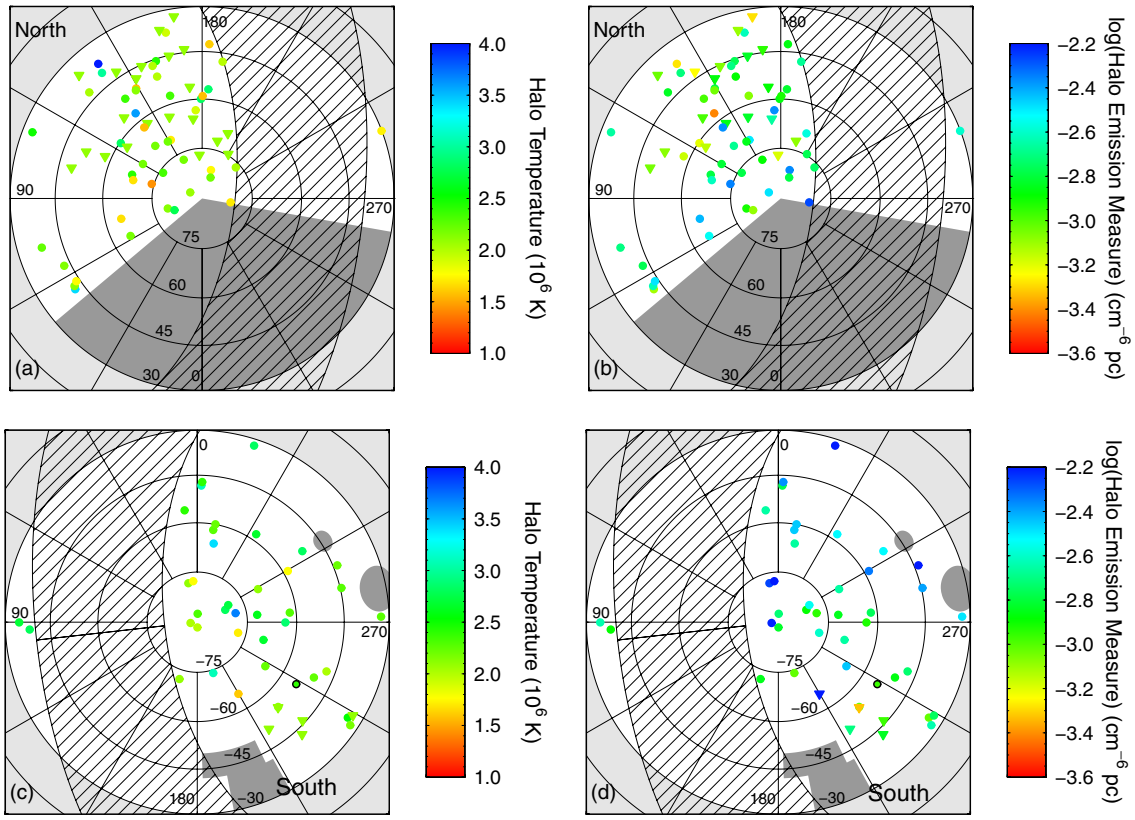

Figure 4. Zenith equal-area maps showing the (a) temperatures and (b) emission measures of the halo in the northern Galactic hemisphere obtained from our spectral modeling. $l = 0°$ is toward the bottom of the figures, and l increases clockwise. The light gray area indicates the region with $|b| \leqslant 30°$, the dark gray area indicates the exclusion region around the Sco-Cen superbubble, and the hatched area indicates the region with $|\beta| \leqslant 20°$. Each of these regions is excluded in this analysis. In the temperature map, the triangles indicate that the temperature was fixed at 2.1×10^6 K. In the emission measure map, the triangles indicate upper limits on the halo emission measure. Panels (c) and (d) show the corresponding results for the southern Galactic hemisphere. Note that $l = 0°$ is toward the top of the figures, and l increases counterclockwise. The dark gray areas indicate the exclusion regions around the Eridanus Enhancement, the Large Magellanic Cloud, and the Small Magellanic Cloud, in order of increasing longitude. Sight line 83, which was analyzed with a $2T$ model (see Section 3.1.2), is outlined in black; we have plotted the results for the cooler ($T \sim (2\text{–}3) \times 10^6$ K) component for this sight line.

(A color version of this figure is available in the online journal.)

Table 3
Correlation Coefficients for Halo Temperature and Emission Measure against Galactic Longitude and Latitude

		Temperature		Emission Measure	
		τ[a]	p-value[b]	τ[a]	p-value[b]
North	$\lvert l\rvert$[c]	−0.07 (−0.27, +0.15)	0.51	−0.17 (−0.28, −0.03)	0.050
	$\lvert b\rvert$	−0.13 (−0.30, +0.05)	0.21	+0.18 (+0.02, +0.29)	0.033
South	$\lvert l\rvert$[c]	−0.22 (−0.42, −0.02)	0.055	−0.44 (−0.55, −0.34)	4.0×10^{-5}
	$\lvert b\rvert$	−0.05 (−0.27, +0.19)	0.65	+0.02 (−0.18, +0.22)	0.82

Notes.
[a] Kendall's τ (e.g., Press et al. 1992), with the 90% bootstrap confidence interval shown in parentheses.
[b] Probability of observing a correlation coefficient at least as extreme as the value that is observed, under the null hypothesis of there being no correlation.
[c] See Equation (2).

There is some evidence (not apparent in the maps in Figure 4) that the halo tends to be slightly hotter in the southern hemisphere than in the northern hemisphere (see rows 4 and 3 of Table 2, respectively). A Mann–Whitney U test (e.g., Barlow 1989; Wall & Jenkins 2003) indicates that the difference in the median temperatures from the two hemispheres is statistically significant at the 1% level ($U = 561$, p-value $= 0.0073$ (two-sided)). We pointed out in Section 4.1 that the region toward the inner Galaxy is excluded in the northern hemisphere but not in the southern hemisphere, which could affect the comparison of the hemispheres. If we exclude the region with $|l| \leqslant 50°$ in the south (Table 2, row 5), we find that the difference in the median temperatures from the two hemispheres is still statistically significant, but now only at the 5% level ($U = 417$, p-value$= 0.027$ (two-sided)). However, it should be noted that the difference is less than the typical error on the temperature ($\sim \pm 0.4 \times 10^6$ K).

There are more non-detections of X-ray emission from the halo in the northern hemisphere than in the south: there are non-detections on 18 out of 66 sight lines (27%) in the north compared with 5 out of 44 sight lines (11%) in the south. However, Fisher's exact test (e.g., Wall & Jenkins 2003) indicates that this difference between the hemispheres is not statistically significant (p-value $= 0.056$ for a two-sided test). A related fact is that the halo emission measure tends to be lower

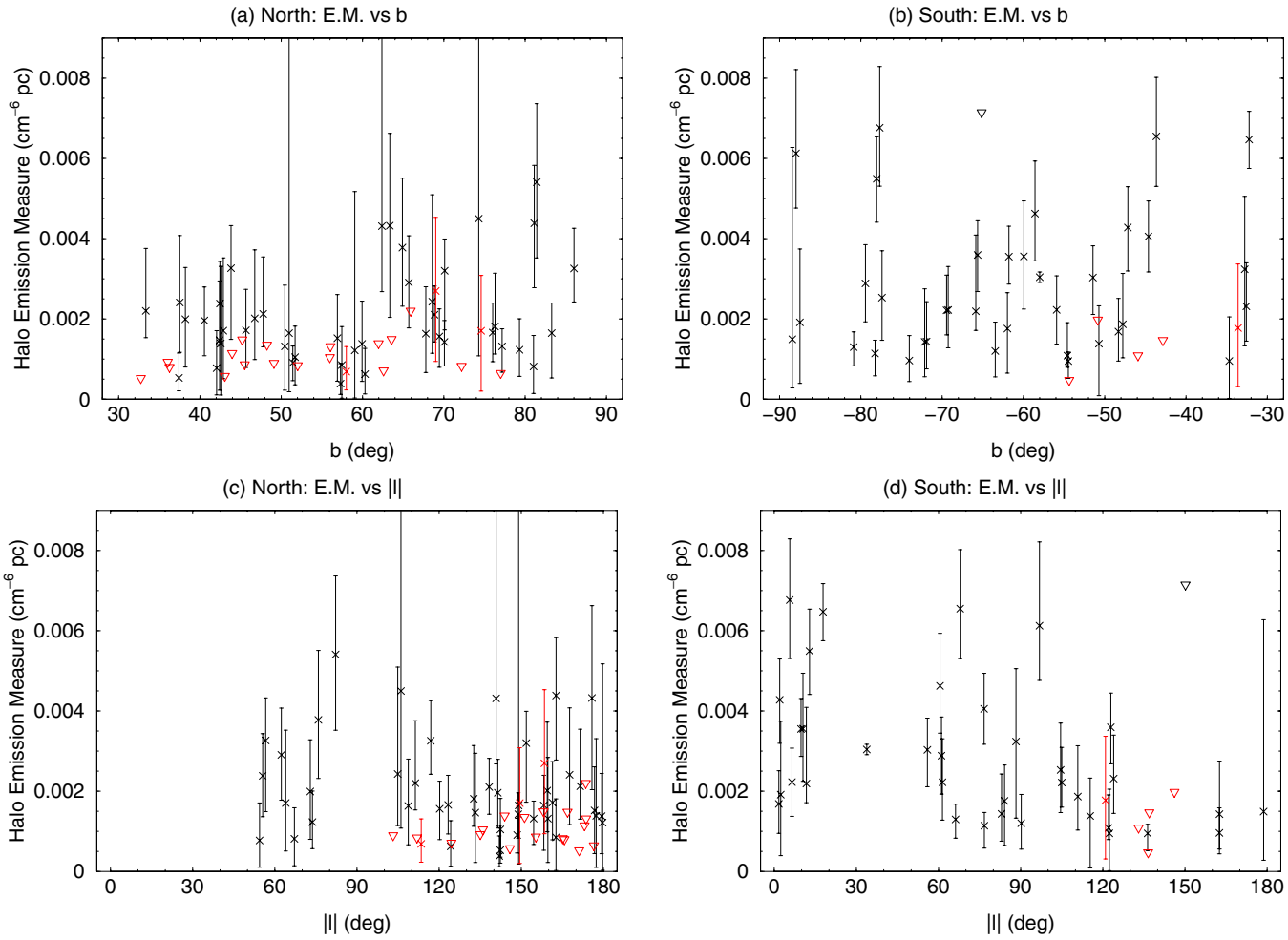

Figure 5. Halo emission measure against (a) b for the northern Galactic hemisphere, (b) b for the southern Galactic hemisphere, (c) $|l|$ for the northern Galactic hemisphere (see Equation (2)), and (d) $|l|$ for the southern Galactic hemisphere. Panels (a) and (d) show the only two examples of statistically significant correlations in Table 3; the other two panels are shown for comparison. Detections are shown with crosses and error bars; upper limits are shown with triangles. The red data points indicate emission measures from sight lines for which the temperature was fixed at 2.1×10^6 K.

(A color version of this figure is available in the online journal.)

in the northern hemisphere than in the south (see rows 3 and 4 of Table 2, respectively). In this case, the difference is significant: the median emission measure in the north is significantly lower than that in the south at the 1% level (Mann–Whitney $U = 971$, p-value $= 0.0034$ (two-sided)). However, this difference between the hemispheres may be due to the exclusion of the region toward the inner Galaxy in the northern hemisphere (note that the emission measure increases toward the inner Galaxy in the southern hemisphere; see Section 4.1). If we exclude the region with $|l| \leqslant 50^\circ$ in the south, the median emission measure in the south (Table 2, row 5) is no longer significantly different from that in the north (Table 2, row 3; $U = 868$, p-value $= 0.10$).

In summary, there is some evidence that the halo temperature and emission measure tend to be somewhat higher in the south than in the north. However, these differences may in part be due to the fact that we do not have data from equivalent regions of the halo in the two hemispheres, as the region toward the inner Galaxy is excluded in the north (because of the presence of the Sco-Cen superbubble).

5. DISCUSSION

In the following subsections, we compare our measurements with those from previous studies, we discuss the effect of our assumed foreground model on our halo measurements, and we consider sources of contamination that could be affecting our halo measurements (Sections 5.1–5.3, respectively). We conclude that contamination and our choice of foreground model are, in general, not adversely affecting our halo measurements. Then, in Section 5.4, we discuss the morphology of the hot halo. Finally, in Section 5.5, we comment on the implications of our measurements for the origin of the hot halo (deferring a more detailed study of this issue to a follow-up paper; D. B. Henley et al., in preparation).

5.1. Comparison with Previous Studies

As noted in Section 2.1, our sample of *XMM-Newton* observations includes 20 that were analyzed in the HSKJM. The halo temperatures that we have measured for these sight lines are generally in good agreement with those measured in HSKJM, and there is no systematic difference in the halo temperatures (although it should be noted that for five of these sight lines we had to fix the halo temperature at 2.1×10^6 K for the current analysis).

The current analysis does, however, yield systematically lower emission measures and surface brightnesses than HSKJM, typically by about a third. Although we use a lower source removal flux threshold than in HSKJM (1×10^{-14} versus $5 \times$

10^{-14} erg cm^{-2} s^{-1}), this appears not to be directly responsible for the difference (i.e., sources with $F_X^{0.5-2.0} = 1 \times 10^{-14}$ to 5×10^{-14} erg cm^{-2} s^{-1} were not contaminating the HSKJM halo measurements). Instead, the difference is most likely due to our using a lower normalization for the extragalactic background (the extragalactic normalization used in HS10 and HSKJM may have been too large, given the source removal threshold). This lower extragalactic normalization results in a higher normalization for the soft proton model, in order to match the observed count rate above ~2 keV. Because of these two components' different spectral shapes, these changes result in more counts below ~1 keV being attributed to the combination of these two components, and hence in fewer counts being attributed to the halo emission (we noted a similar effect in HS12 when we compared our oxygen intensity measurements with those from HS10). Therefore, the presence of the soft proton contamination in the *XMM-Newton* spectra, which requires us to fix the normalization of the extragalactic background, potentially introduces some uncertainty in the normalization of the halo X-ray emission.

In Figure 6, we compare our *XMM-Newton* halo measurements with *Suzaku* halo measurements from the literature. We have plotted our temperature and emission measure measurements, along with the values measured by Yoshino et al. (2009) from 11 high-latitude *Suzaku* observations (the largest study of the SXRB with *Suzaku* to date). We also plot the temperature and emission measure found by Gupta et al. (2009) from their *Suzaku* shadowing study of MBM 20—we included this data point so that we could compare different methods for determining the foreground emission (see Section 5.2). Note that the observations used by Smith et al. (2007b) and Lei et al. (2009) in their *Suzaku* shadowing analyses are included in the Yoshino et al. (2009) data set, and so we do not include Smith et al.'s or Lei et al.'s results in Figure 6.

The ranges of temperatures and emission measures measured by Yoshino et al. (2009) and Gupta et al. (2009) are generally similar to ours, although our data set includes several sight lines with $T < 2 \times 10^6$ K, which the *Suzaku* data set does not. While the median temperature (2.43×10^6 K) and median emission measure (2.62×10^{-3} cm^{-6} pc) from the combined Yoshino et al. and Gupta et al. data set are both somewhat higher than our median detected values (2.22×10^6 K and 1.91×10^{-3} cm^{-6} pc, respectively; Table 2, row 1), Mann–Whitney U tests indicate that these differences are not statistically significant ($U = 638$ and 654, with two-sided p-values of 0.14 and 0.16 for the temperature and emission measure, respectively). Note that there is one sight line that features in both our data set (sight line 12) and in Yoshino et al. (2009, their sight line 1) on which the measured halo temperatures are $(1.68^{+0.30}_{-0.25}) \times 10^6$ and $(2.58^{+1.29}_{-0.79}) \times 10^6$ K, respectively. Although this discrepancy is rather large, the 90% confidence intervals do overlap. Furthermore, the Yoshino et al. confidence interval does not seem to include an estimate of the systematic error due to their assumed foreground model. Thus, for this sight line, the temperature discrepancy is not significant given the measurement errors.

In addition to comparing the temperatures and emission measures from the *XMM-Newton* and *Suzaku* data sets, we can use the temperatures and emission measures from Yoshino et al. (2009) and Gupta et al. (2009) to calculate the intrinsic 0.5–2.0 keV halo surface brightnesses implied by their best-fit models, for comparison with our surface brightness measurements. For the Yoshino et al. (2009) sight lines, we also take

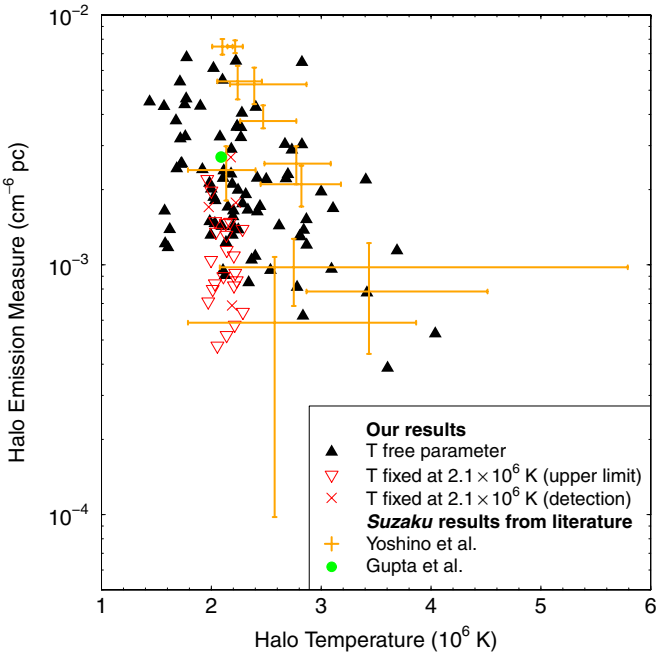

Figure 6. Comparison of our halo results with those obtained from *Suzaku* SXRB spectra. Our results are generally plotted with black triangles, with the error bars omitted. If the temperature was fixed at 2.1×10^6 K, the results are plotted with red triangles and red crosses, for upper limits and detections, respectively. As in Figure 3, the red data points have been staggered in the horizontal direction from $T = 2.1 \times 10^6$ K, in order to reduce clutter. The results from the Yoshino et al. (2009) *Suzaku* study are plotted with orange crosses (from their Table 6). We only show Yoshino et al.'s measurements of the ~(2–3) $\times 10^6$ K halo; we do not plot the results for the hotter halo component from their Table 7. We have omitted the low-latitude LL10 sight line, and sight line LH-2, on which halo emission is not detected. The light green circle near $T = 2 \times 10^6$ K, emission measure $= 3 \times 10^{-3}$ cm^{-6} pc shows the result from the *Suzaku* shadowing observation of MBM 20 (Gupta et al. 2009).

(A color version of this figure is available in the online journal.)

into account the non-solar Fe/O and Ne/O ratios (from their Table 6). While the halo temperatures and emission measures obtained with *Suzaku* are in good overall agreement with our measurements, the median surface brightness inferred from the best-fit *Suzaku* models is significantly higher than the value from our analysis, although only at the 5% level (2.68×10^{-12} versus 1.54×10^{-12} erg cm^{-2} s^{-1} deg^{-2}; Mann–Whitney $U = 735$, p-value $= 0.023$ (two-sided)). However, it should be noted that the supersolar Fe/O and Ne/O ratios on some of Yoshino et al.'s sight lines lead to enhanced halo emission at energies $\gtrsim$0.8 keV (see their Figure 5, and compare with our Figure 1). If there is such harder emission from the halo, our solar-abundance 1T halo models are unable to model it, and so our models would tend to yield lower total halo surface brightnesses. (We did experiment with non-solar Fe/O and Ne/O ratios, but found that in general we were unable to obtain reliable results.)

Above, we noted that the presence of the soft proton contamination in the *XMM-Newton* spectra potentially introduces some uncertainty in the normalization of the halo X-ray emission. In general, our halo measurements and those obtained with *Suzaku* (which does not suffer from soft proton contamination) are in reasonable agreement. This suggests that, in practice, soft proton contamination is not a major source of bias.

It should be noted that our best-fit halo models attribute somewhat less R45 (3/4 keV) emission to the Galactic halo than Kuntz & Snowden's (2000) analysis of the *ROSAT* All-Sky Survey. For sight lines on which emission is detected,

our best-fit models typically imply observed halo R45 count rates of (18–49) $\times 10^{-6}$ counts s^{-1} arcmin^{-2} (median = 27×10^{-6} counts s^{-1} arcmin^{-2}). In contrast, Kuntz & Snowden (2000) inferred an observed halo R45 count rate of 38.6×10^{-6} counts s^{-1} arcmin^{-2} in the vicinity of the northern Galactic pole (their Table 2: "Remainder"−"Stars"). However, the uncertainty on the Kuntz & Snowden (2000) halo R45 count rate is not stated, so we are unable to determine whether or not this discrepancy is significant.

5.2. Effect of the Foreground Model

Here, we consider the choice of the foreground component in the SXRB model as another potential source of uncertainty in the determination of the halo emission. The normalization and spectral shape of the foreground component may affect the emission measure and temperature measured for the halo plasma. In our analysis, we followed HSKJM, and used shadowing data from the *ROSAT* All-Sky Survey (Snowden et al. 2000) to fix our foreground model. This method requires extrapolating the foreground model from the *ROSAT* 1/4 keV band to the *XMM-Newton* band ($E \geqslant 0.4$ keV). If this extrapolation leads to an inaccurate foreground model in the *XMM-Newton* band, it will bias our measurements of the halo temperature and emission measure.

The above-mentioned *Suzaku* measurements used different techniques for estimating the foreground emission. Yoshino et al. (2009) found a tight correlation between the observed O VII and O VIII intensities in their sample of spectra, with a non-zero "floor" to the O VII emission, leading them to conclude that their spectra included a uniform local component with O VII and O VIII intensities of ∼2 and ∼0 photons cm^{-2} s^{-1} sr^{-1}, respectively. They subsequently used a foreground model with these oxygen intensities to obtain their halo measurements. Gupta et al. (2009), meanwhile, compared the emission toward and to the side of the shadow cast in the SXRB by MBM 20, and thus inferred the contributions to the emission originating in front of and behind the shadowing cloud. The reasonable agreement between our measurements and these *Suzaku* measurements suggests that, in fact, our choice of foreground model is not adversely affecting our halo measurements.

D. B. Henley & R. L. Shelton (in preparation) adopt a novel, Bayesian approach to inferring the halo X-ray emission from the HS12 *XMM-Newton* SXRB survey. They first use the observed time variation of the oxygen intensities in directions that have been observed multiple times to specify the prior probability distribution for the time-variable SWCX intensity in an arbitrary *XMM-Newton* observation. They then combine this prior with oxygen intensities from other directions to constrain the posterior probability distribution for the intrinsic halo emission. This new technique yields combined O VII + O VIII halo surface brightnesses that are generally in reasonable agreement with those inferred from the best-fit halo models in this paper. However, the halo temperatures inferred from the O VIII/O VII ratios are typically $\sim 0.4 \times 10^6$ K lower than those in this paper.

When D. B. Henley & R. L. Shelton (in preparation) compare the observations that are included both in that analysis and in the current analysis, they find that their analysis tends to attribute more O VIII emission to the foreground than our current foreground model (our foreground model, with $T = 1.2 \times 10^6$ K (Section 3.1.1), produces virtually no O VIII emission, which is consistent with Yoshino et al.'s (2009) foreground model). This results in less O VIII emission being attributed to the halo, and hence in a lower temperature being inferred from the O VIII/O VII ratio.

D. B. Henley & R. L. Shelton (in preparation) repeat our spectral analysis with a higher-temperature foreground model, chosen to better match the foreground O VIII intensities inferred from their analysis. This revised foreground model results in halo temperatures that are lower than those presented here, and in better agreement with those inferred from the D. B. Henley & R. L. Shelton (in preparation) O VIII/O VII ratios. This may imply that we (and Yoshino et al. 2009; and Gupta et al. 2009) are underestimating the foreground O VIII intensity in our spectral fitting, and thus overestimating the halo temperature. However, D. B. Henley & R. L. Shelton (in preparation) also point out that the halo emission likely originates from plasma with a range of temperatures and in a range of ionization states. If this is the case, the spectral fitting described here will not necessarily arrive at the same best-fit halo temperature as that inferred from the O VIII/O VII ratio alone.

In summary, after comparing our results with those from other studies which use a variety of methods for determining the foreground emission (Yoshino et al. 2009; Gupta et al. 2009; D. B. Henley & R. L. Shelton, in preparation), we conclude that our choice of foreground model is not seriously biasing our measurements of the halo surface brightness. Similarly, our halo temperatures agree with those from other studies that use spectral fitting (Yoshino et al. 2009; Gupta et al. 2009). However, our temperatures are higher than those inferred from the halo O VIII/O VII ratios determined using a novel, Bayesian approach to constraining the halo emission (D. B. Henley & R. L. Shelton, in preparation). While this discrepancy may in part be due to our underestimating the foreground O VIII intensity, it may also be due to the fact that the halo likely has a complicated temperature and ionization structure, so different methods of characterizing the halo emission may yield different temperatures. Despite this, such temperature measurements are still useful for testing halo models, provided the predicted halo emission is treated like the true halo emission. This involves creating synthetic observations from the predicted halo spectra, which are then analyzed with the same SXRB model as the real observations (HSKJM).

5.3. Possible Contamination of the Halo Emission

In Section 5.1, we argued that soft proton contamination was unlikely to be significantly biasing our results. This conclusion is supported by the fact that we find no correlation between our measured halo parameters and the level of soft proton contamination, as quantified by the ratio of the total 2–5 keV model flux to that expected from the extragalactic background, $F^{2-5}_{\rm total}/F^{2-5}_{\rm exgal}$ (introduced in HS10). For this purpose, we used HS12's measurements of $F^{2-5}_{\rm total}/F^{2-5}_{\rm exgal}$, from their Table 2.

SWCX emission is also unlikely to be adversely affecting our halo measurements: our observations were selected from HS12's catalog as they were expected to be the least contaminated by SWCX emission (Section 2.1), and in Section 5.2 we argued that our choice of foreground model is not seriously biasing our measurements of the halo surface brightness. In this subsection, we consider other potential sources of contamination.

Our halo measurements are unlikely to be contaminated by emission from the original targets of the *XMM-Newton* observations. In HS12, we experimented with increasing the radii of the exclusion regions used to excise the *XMM-Newton*

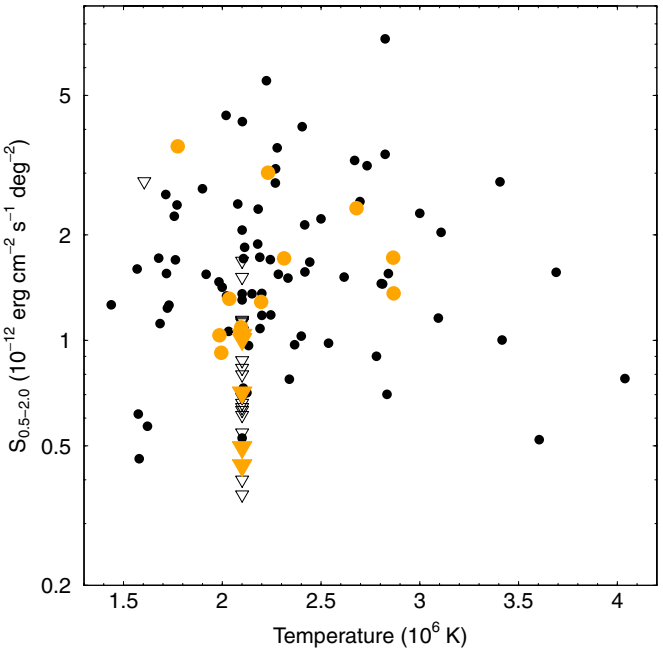

Figure 7. 0.5–2.0 keV halo surface brightnesses against halo temperatures. Sight lines on which the original target of the *XMM-Newton* observation was a galaxy cluster are colored orange. The triangles indicate upper limits on the surface brightnesses.

(A color version of this figure is available in the online journal.)

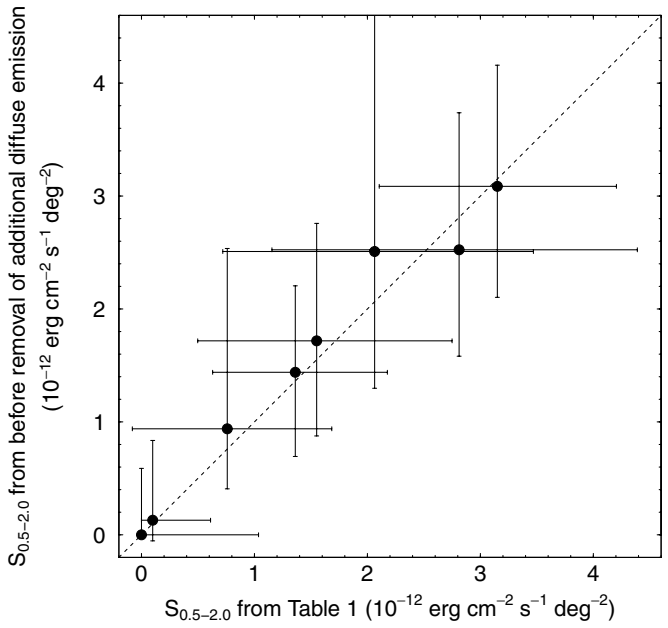

Figure 8. 0.5–2.0 keV surface brightnesses of the $\sim(2–3) \times 10^6$ K halo emission measured before (ordinates) and after (abscissae) removing regions of diffuse emission that had not been removed in HS12 (see Section 2.2). We have plotted the results for the sight lines indicated by a "d" in Column 1 of Table 1 (apart from sight line 83). These sight lines yielded a halo temperature of $\sim 10 \times 10^6$ K when we used the HS12 exclusion regions, but a temperature of $\sim(2–3) \times 10^6$ K after removing additional regions of diffuse emission. The ordinates were obtained by analyzing the originally extracted SXRB spectra with a $2T$ model to model the non-foreground, non-extragalactic-background emission—the plotted values are for the cooler component of this model.

target objects, and concluded that the SXRB O VII and O VIII intensities were not being contaminated by emission from those targets (see Section 3.6 of HS12). Since the O VII and O VIII emission dominates the halo emission in the *XMM-Newton* band, the results from HS12 imply that our halo measurements are not contaminated by emission from the *XMM-Newton* targets.

In Figure 7, we compare the results from sight lines on which the target object was a galaxy cluster (orange) with those from other sight lines (black). We single out galaxy clusters because it can be difficult to determine the extent of the cluster emission from a visual inspection of the X-ray images, and so emission from the cluster periphery could potentially contaminate our halo measurements. However, Figure 7 shows that the halo surface brightnesses measured on cluster sight lines are not systematically higher than those on other sight lines. For sight lines on which halo emission is detected, the median surface brightnesses on cluster and non-cluster sight lines are 1.36×10^{-12} and 1.55×10^{-12} erg cm^{-2} s^{-1} deg^{-2}, respectively. We therefore conclude that emission from the peripheries of targeted galaxy clusters is not contaminating our halo measurements.

Our halo measurements could also potentially be contaminated by non-targeted galaxy groups or clusters that happen to lie in the *XMM-Newton* fields of view. Unless such objects are particularly bright, they may have escaped being noticed in our visual inspection of the X-ray images. Indeed, in Section 2.2, we noted that when we used the exclusion regions used in HS10 and HS12, our initial spectral fitting yielded unusually high halo temperatures on nine sight lines ($T \sim 10 \times 10^6$ K). Upon re-examination of these sight lines, using newly created adaptively smoothed, QPB-subtracted images, we found additional diffuse emission that had not been adequately removed after the initial visual inspection. After removing these additional regions of diffuse emission, the spectral fitting generally yielded typical halo temperatures for these sight lines ($T \sim (2–3) \times 10^6$ K).

It is likely that similar regions of diffuse emission lie in the other fields of view, which we have not re-examined. However, such regions are unlikely to be contaminating our halo measurements. Before removing the additional regions of diffuse emission from the nine sight lines noted above, we analyzed the SXRB spectra using a $2T$ model to model the non-foreground, non-extragalactic-background emission: one component to model the $\sim(2–3) \times 10^6$ K halo emission, and a $\sim 10 \times 10^6$ K component of uncertain origin. The properties of the cooler component from before the removal of the additional regions of diffuse emission and the properties of the halo component from after the removal of said regions are consistent with each other. In particular, the surface brightnesses of the $\sim(2–3) \times 10^6$ K emission were not greatly affected (see Figure 8). We therefore conclude that non-targeted extragalactic diffuse emission that happens to lie in our remaining *XMM-Newton* fields of view is not contaminating our halo measurements. At least in part, this is likely because galaxy groups and clusters tend to be much hotter than $\sim(2–3) \times 10^6$ K (e.g., Osmond & Ponman 2004; Sanderson et al. 2003).

Finally, we consider contamination from point sources. The combined flux from point sources below our source removal flux threshold ($F_X^{0.5-2.0} = 1 \times 10^{-14}$ erg cm^{-2} s^{-1}) is modeled by our extragalactic background model (Section 3.1.3). Our estimates of the systematic errors take into account the uncertainty in the normalization of the extragalactic background (Section 3.2). Although the uncertainty in the normalization of the extragalactic background is $\pm 1.1 \times 10^{-12}$ erg cm^{-2} s^{-1} deg^{-2} (Section 3.2), we find that this leads to an uncertainty in the halo surface

brightness typically of only $\pm 0.3 \times 10^{-12}$ erg cm^{-2} s^{-1} deg^{-2}. Somewhat surprisingly, increasing the brightness of the extragalactic background from its nominal value generally leads to an increase in the halo surface brightness. This is because increasing the brightness of the extragalactic background causes the soft proton component to decrease in brightness to compensate, and the combination of these effects leads to more flux being attributed to the halo emission (see Section 5.1).

Sources brighter than the above threshold were excised in the automated source removal (Section 2.2), using circles of radius 50′, which enclose ≈90% of each source's flux.[7] (The brighter sources were removed with larger source exclusion regions, positioned by eye over the sources.) Using the source fluxes either from the *XMM-Newton* Serendipitous Source Catalog or from the source detection that we ran ourselves, we can estimate the total flux in each field due to photons from automatically removed sources that have spilled out of the source exclusion regions. Typically, this flux is $<0.5 \times 10^{-12}$ erg cm^{-2} s^{-1} deg^{-2}. This is less than the uncertainty in the normalization of the extragalactic background, and the effect of this contaminating flux on the halo surface brightnesses is likely to be small (as noted above, the uncertainty in the extragalactic normalization leads to an uncertainty in the halo surface brightness typically of only $\pm 0.3 \times 10^{-12}$ erg cm^{-2} s^{-1} deg^{-2}).

In summary, our halo measurements are unlikely to be significantly affected by contamination from the original *XMM-Newton* targets, from non-targeted group or clusters of galaxies lying in the fields of view, or from photons spilling out of the source exclusion regions defined in the automated source removal.

5.4. The Morphology of the Hot Galactic Halo

While the halo temperature appears to be fairly uniform, the halo emission measure exhibits considerable variation across the sky (Figure 4). In Section 4.1, we showed that the halo emission measure tends to increase from the outer to the inner Galaxy, at least in the southern Galactic hemisphere. We previously noted a similar trend for the *observed* O VII and O VIII intensities in the south (HS12). Since the SWCX intensity is not expected to be correlated with Galactic longitude, we argued in HS12 (Section 4.3.1) that the observed trend reflected an increase in the halo's *intrinsic* emission from the outer to the inner Galaxy, in agreement with the halo measurements presented here. These results argue against the hot halo having a simple plane-parallel disk-like morphology, in which case the emission measure would be independent of Galactic longitude. Instead, these results suggest a halo that is concentrated toward the Galactic center.

The variation (or lack thereof) of the halo emission measure with latitude is also different from that expected for a plane-parallel disk-like halo morphology. In such a morphology, the emission measure is expected to decrease with latitude as $1/\sin|b|$. Instead, we find the halo emission measure to weakly increase with latitude in the north, and to be uncorrelated with latitude in the south (see Table 3, and Figures 5(a) and (b)). Similarly, we previously found that our SXRB oxygen intensity measurements argued against a plane-parallel halo model in the northern Galactic hemisphere (see HS12, Section 4.3.3).

Yoshino et al. (2009) did find that the halo emission measure decreased with latitude. However, the decrease with latitude is steeper than that expected for a plane-parallel model (see their Figure 7; EM $\times \sin|b|$ is expected to be constant for a plane-parallel model). Note also that the Yoshino et al. (2009) data set contains far fewer sight lines than ours. The fact that our halo emission measures do not decrease with increasing latitude, contrary to what is expected for a disk-like halo morphology, and contrary to the Yoshino et al. (2009) *Suzaku* results, is unlikely to be due to soft proton contamination (a problem from which *Suzaku* does not suffer). We argued in Sections 5.1 and 5.3 that such contamination does not seriously bias our halo emission measures.

The fact that our halo emission measures do not decrease with increasing latitude is also unlikely to be due to our using H I column densities to attenuate the halo emission. By using such column densities, we could potentially be neglecting the contributions to the absorption from regions containing H II or molecular H. For each sight line, we extracted the interstellar reddening, $E(B-V)$, from the Schlegel et al. (1998) maps (derived from *COBE*/DIRBE-corrected *IRAS* data), and converted to $N_{\rm H}$ using the conversion relation from Güver & Özel (2009). This relation was derived from X-ray spectral analysis of SN remnants, and hence should yield the total hydrogen column density (although note that the hydrogen column densities in that study are typically larger than those used in the present paper). Surprisingly, the hydrogen column densities obtained in this way were typically *smaller* than the H I column densities. Furthermore, the effect on the attenuation factor ($\exp(-\sigma N_{\rm H})$, where σ is the photoelectric absorption cross section) was typically less than a few percent in the vicinity of the oxygen lines, and uncorrelated with latitude. Hence, our using H I column densities is unlikely to be responsible for our emission measure measurements not following the trend expected for a disk-like halo morphology. Note also that Yoshino et al. (2009) used H I column densities for all but two of their sight lines.

In summary, our observations suggest that the halo is concentrated toward the Galactic center. Other than that, the morphology of the hot halo remains uncertain. However, our observed emission measures do not vary with latitude in the way expected for a disk-like halo morphology. The patchiness of the halo emission makes it difficult to determine the halo's underlying global morphology.

5.5. The Origin of the Hot Galactic Halo

We defer a detailed comparison of our observations to models of the hot halo to a follow-up paper (D. B. Henley et al., in preparation). However, here we make some general comments on the implications of our results for the origin of the hot halo.

We cannot use energy arguments to distinguish between SN-driven outflows and accretion of extragalactic material as the sources of the hot halo plasma, since both processes have more than enough energy to power the X-ray emission. The latitude-corrected intrinsic halo surface brightness, $S_{0.5\text{–}2.0}\sin|b|$, implies a 0.5–2.0 keV halo luminosity of $8\pi S_{0.5\text{–}2.0}\sin|b| = 8.4 \times 10^{35}$ erg s^{-1} kpc^{-2} (where we have used the median of $S_{0.5\text{–}2.0}\sin|b|$, 1.07×10^{-12} erg cm^{-2} s^{-1} deg^{-2}, including non-detections at their best-fit values). As has previously been noted, this is much less than the energy available from SNe (8×10^{38} erg s^{-1} kpc^{-2}; e.g., Yao et al. 2009). It is also

[7] This encircled energy fraction, which depends only weakly on the off-axis angle, was calculated from the best-fit King profiles to the MOS telescopes' point-spread functions, using the `XRT1_XPSF_0014.CCF` and `XRT2_XPSF_0014.CCF` calibration files (see the *XMM-Newton* Calibration Access and Data Handbook; http://xmm.vilspa.esa.es/external/xmm_sw_cal/calib/documentation/CALHB/node30.html).

much less than the energy potentially available from accretion. The Galactic escape speed in the vicinity of the Sun (540 km s^{-1}; Smith et al. 2007a) implies a gravitational potential of -1.5×10^{15} erg g^{-1}. If the Galaxy accretes mass at a rate of $\sim 0.4\, M_{\odot}\ yr^{-1}$ (Chiappini 2009) over a disk of radius $\sim$20 kpc, $\sim 3 \times 10^{37}$ erg s^{-1} kpc^{-2} is available from accretion in the vicinity of the Sun.[8] Detailed models of the outflow and accretion scenarios are needed to determine how much of the available energy is actually radiated as X-rays.

In Section 5.4, we pointed out that our and HS12's measurements suggest a halo that is concentrated toward the Galactic center. Such a morphology may be due to a halo of accreted material centered on the Galactic center, or to an increase in the Galactic SN rate toward the inner Galaxy (e.g., the SN rate per unit area increases by a factor of $\sim$20 from 2 kpc outside the solar circle to 2 kpc within the solar circle; Ferrière 1998).

We noted in Section 4 that the halo emission measure and intrinsic surface brightness vary by an order of magnitude over the sky, while the temperature is fairly uniform (see Figure 3). Figures 4(b) and (d) show that the halo emission is patchy (Yoshino et al. 2009; HS10; HSKJM). Such patchiness may favor a stochastic, inhomogeneous energy source, such as SNe, as the source of the hot halo (HSKJM). However, if accreting extragalactic material fragments as it accretes, it too could lead to patchy emission.

In summary, arguments can be made in favor of both the outflow and the accretion scenarios based on our current set of observations. Detailed models are needed to determine which of these processes dominate the X-ray emission, or if both processes play a significant role. Not only should such models match the observed X-ray temperature and surface brightness, but ideally they should also explain the observed variation in the halo brightness—both the general increase from the inner to the outer Galaxy and the patchiness of the emission.

6. SUMMARY

We have presented measurements of the Galactic halo's X-ray emission on 110 *XMM-Newton* sight lines. This is an approximately fourfold increase in the number of sight lines over the previous largest study of the Galactic halo with CCD-resolution X-ray spectra (HSKJM). Our sample of observations is drawn from an *XMM-Newton* survey of the SXRB (HS12). We selected these observations as they should be the least contaminated by charge exchange emission from within the solar system. We analyzed the spectra with a standard SXRB model, with components representing the foreground, Galactic halo, and extragalactic background emission.

We detected emission from $\sim$(2–3) $\times 10^6$ K plasma on 87 of our sight lines (79%), with typical emission measures of (1.4–3.0) $\times 10^{-3}$ cm^{-6} pc, and typical intrinsic 0.5–2.0 keV surface brightnesses of (1.1–2.3) $\times 10^{-12}$ erg cm^{-2} s^{-1} deg^{-2} (Section 4). The halo emission measure tends to increase from the outer to the inner Galaxy in the southern Galactic hemisphere (Section 4.1). There is some evidence that the halo is hotter and has a larger emission measure in the southern hemisphere than in the north (Section 4.2). However, the differences may be partly due to the fact that we are not comparing equivalent regions in both hemispheres. Because of the presence of the Sco-Cen superbubble, we excluded the region toward the inner Galaxy in the northern hemisphere but not in the south, and, as noted above, the emission measure increases toward the inner Galaxy in the south. In addition, it should be noted that the difference in the median temperature between the hemispheres ($\sim 0.2 \times 10^6$ K) is less than the typical error on the temperature ($\sim \pm 0.4 \times 10^6$ K).

Our halo emission measures and surface brightnesses are in reasonable agreement with those measured with *Suzaku* (Yoshino et al. 2009; Gupta et al. 2009) (Section 5.1). Similarly, the halo surface brightnesses attributable to the oxygen Kα lines (derived from our best-fit halo models) are generally in reasonable agreement with those derived from a Bayesian analysis of the oxygen intensities from the HS12 *XMM-Newton* SXRB survey (D. B. Henley & R. L. Shelton, in preparation) (Section 5.2). Since these studies all used different methods for estimating the foreground emission, and since *Suzaku* does not suffer from significant soft proton contamination, we conclude that neither our choice of foreground model nor soft proton contamination significantly biases our halo surface brightness measurements. Contamination from the original targets of the *XMM-Newton* observations, from non-targeted galaxy groups and clusters lying in the fields of view, and from point sources is also not significantly affecting our measurements (Section 5.3).

Our halo temperatures are in agreement with those measured with *Suzaku*, but are higher than those inferred from the halo O VIII/O VII ratios determined from the above-mentioned Bayesian analysis of the SXRB oxygen lines (D. B. Henley & R. L. Shelton, in preparation). In Section 5.2, we mentioned two possible explanations for this discrepancy. The discrepancy may indicate that we (and the *Suzaku* studies) are underestimating the foreground O VIII intensity, thus biasing the halo measurements. Alternatively, the discrepancy may be due to the halo having a complex multitemperature, multi-ionization-state structure, meaning that the O VIII/O VII ratio and the broadband spectral analysis will not necessarily yield the same best-fit temperature.

Our halo emission measures do not decrease with increasing Galactic latitude, contrary to what is expected for a plane-parallel disk-like halo morphology. This result appears not to be an artifact of soft proton contamination, nor of our using H I column densities when calculating the attenuation of the halo emission. The details of the morphology of the halo remain uncertain, but the variation of the emission measure with longitude suggests that the halo is concentrated toward the Galactic center (Section 5.4).

We are unable to distinguish between extragalactic accretion and outflows from the disk as the source of the $\sim$(2–3) $\times 10^6$ K halo plasma. Both processes have more than enough energy to maintain the halo's surface brightness, and other aspects of the halo emission (such as the increase in emission measure toward the inner Galaxy and the general patchiness of the emission) could plausibly be explained by either scenario (Section 5.5). A detailed comparison of our measurements with the predictions of hydrodynamical models of the halo is needed to distinguish between different scenarios for the heating of the halo. We will carry out such a comparison in a follow-up paper (D. B. Henley et al., in preparation).

We thank the anonymous referee, whose comments helped significantly improve this paper. This research is based on observations obtained with *XMM-Newton*, an ESA science mission with instruments and contributions directly funded by ESA Member States and NASA. We acknowledge use of the R software package (R Development Core Team 2008). This

[8] Of course, the hot gas observed in the halo has not fallen all the way to the Sun. However, integrating the vertical gravitational acceleration at the solar circle (Ferrière 1998) to a height of 3 kpc, we find that the estimate of the available energy need only be revised downward by a few percent for hot gas a few kpc above the disk.

research has made use of the SIMBAD database, operated at CDS, Strasbourg, France, and of the NASA/IPAC Extragalactic Database (NED), which is operated by the Jet Propulsion Laboratory, California Institute of Technology, under contract with the National Aeronautics and Space Administration. This research was funded by NASA grant NNX08AJ47G, awarded through the Astrophysics Data Analysis Program.

REFERENCES

Anders, E., & Grevesse, N. 1989, GeCoA, 53, 197
Bałucińska-Church, M., & McCammon, D. 1992, ApJ, 400, 699
Barlow, R. 1989, Statistics: A Guide to the Use of Statistical Methods in the Physical Sciences (Chichester: Wiley)
Bregman, J. N. 1980, ApJ, 236, 577
Bregman, J. N., & Lloyd-Davies, E. J. 2007, ApJ, 669, 990
Burrows, D. N., & Mendenhall, J. A. 1991, Natur, 351, 629
Burrows, D. N., Singh, K. P., Nousek, J. A., Garmire, G. P., & Good, J. 1993, ApJ, 406, 97
Carter, J. A., & Sembay, S. 2008, A&A, 489, 837
Carter, J. A., Sembay, S., & Read, A. M. 2010, MNRAS, 402, 867
Carter, J. A., Sembay, S., & Read, A. M. 2011, A&A, 527, A115
Chen, L.-W., Fabian, A. C., & Gendreau, K. C. 1997, MNRAS, 285, 449
Chiappini, C. 2009, in Proc. IAU Symp. 254, The Galaxy Disk in Cosmological Context, ed. J. Andersen, J. Bland-Hawthorn, & B. Nordström (Cambridge: Cambridge Univ. Press), 191
Crain, R. A., McCarthy, I. G., Frenk, C. S., Theuns, T., & Schaye, J. 2010, MNRAS, 407, 1403
Cravens, T. E. 2000, ApJL, 532, L153
Cravens, T. E., Robertson, I. P., & Snowden, S. L. 2001, JGR, 106, 24883
Egger, R. J., & Aschenbach, B. 1995, A&A, 294, L25
Ezoe, Y., Ebisawa, K., Yamasaki, N. Y., et al. 2010, PASJ, 62, 981
Ezoe, Y., Miyoshi, Y., Yoshitake, H., et al. 2011, PASJ, 63, S691
Fang, T., Bullock, J., & Boylan-Kolchin, M. 2013, ApJ, 762, 20
Fang, T., McKee, C. F., Canizares, C. R., & Wolfire, M. 2006, ApJ, 644, 174
Fang, T., Sembach, K. R., & Canizares, C. R. 2003, ApJL, 586, L49
Ferrière, K. 1998, ApJ, 497, 759
Fujimoto, R., Mitsuda, K., McCammon, D., et al. 2007, PASJ, 59, S133
Galeazzi, M., Gupta, A., Covey, K., & Ursino, E. 2007, ApJ, 658, 1081
Gupta, A., & Galeazzi, M. 2009, ApJ, 702, 270
Gupta, A., Galeazzi, M., Koutroumpa, D., Smith, R., & Lallement, R. 2009, ApJ, 707, 644
Gupta, A., Mathur, S., Krongold, Y., Nicastro, F., & Galeazzi, M. 2012, ApJL, 756, L8
Güver, T., & Özel, F. 2009, MNRAS, 400, 2050
Hagihara, T., Yao, Y., Yamasaki, N. Y., et al. 2010, PASJ, 62, 723
Hasinger, G., Burg, R., Giacconi, R., et al. 1993, A&A, 275, 1
Henley, D. B., & Shelton, R. L. 2008, ApJ, 676, 335
Henley, D. B., & Shelton, R. L. 2010, ApJS, 187, 388 (HS10)
Henley, D. B., & Shelton, R. L. 2012, ApJS, 202, 14 (HS12)
Henley, D. B., Shelton, R. L., Kwak, K., Joung, M. R., & Mac Low, M.-M. 2010, ApJ, 723, 935 (HSKJM)
Hickox, R. C., & Markevitch, M. 2006, ApJ, 645, 95
Joung, M. K. R., & Mac Low, M.-M. 2006, ApJ, 653, 1266
Kalberla, P. M. W., Burton, W. B., Hartmann, D., et al. 2005, A&A, 440, 775
Koutroumpa, D., Acero, F., Lallement, R., Ballet, J., & Kharchenko, V. 2007, A&A, 475, 901
Koutroumpa, D., Lallement, R., Kharchenko, V., et al. 2006, A&A, 460, 289
Kuntz, K. D., & Snowden, S. L. 2000, ApJ, 543, 195
Kuntz, K. D., & Snowden, S. L. 2008, A&A, 478, 575
Lampton, M., Margon, B., & Bowyer, S. 1976, ApJ, 208, 177
Lei, S., Shelton, R. L., & Henley, D. B. 2009, ApJ, 699, 1891
Marshall, F. J., Boldt, E. A., Holt, S. S., et al. 1980, ApJ, 235, 4
McCammon, D., & Sanders, W. T. 1990, ARA&A, 28, 657
McKernan, B., Yaqoob, T., & Reynolds, C. S. 2004, ApJ, 617, 232
Moretti, A., Campana, S., Lazzati, D., & Tagliaferri, G. 2003, ApJ, 588, 696
Nicastro, F., Zezas, A., Drake, J., et al. 2002, ApJ, 573, 157
Norman, C. A., & Ikeuchi, S. 1989, ApJ, 345, 372
Osmond, J. P. F., & Ponman, T. J. 2004, MNRAS, 350, 1511
Peebles, P. J. E. 1980, The Large-Scale Structure of the Universe (Princeton, NJ: Princeton Univ. Press)
Pietz, J., Kerp, J., Kalberla, P. M. W., et al. 1998, A&A, 332, 55
Press, W. H., Teukolsky, S. A., Vetterling, W. T., & Flannery, B. P. 1992, Numerical Recipes in C—The Art of Scientific Computing (2nd ed.; Cambridge: Cambridge Univ. Press)
R Development Core Team. 2008, R: A Language and Environment for Statistical Computing (Vienna, Austria: R Foundation for Statistical Computing)
Rasmussen, A., Kahn, S. M., & Paerels, F. 2003, in The IGM/Galaxy Connection. The Distribution of Baryons at $z = 0$, ed. J. L. Rosenberg & M. E. Putman (Dordrecht: Kluwer), 109
Rasmussen, J., Sommer-Larsen, J., Pedersen, K., et al. 2009, ApJ, 697, 79
Raymond, J. C., & Smith, B. W. 1977, ApJS, 35, 419
Roberts, T. P., & Warwick, R. S. 2001, in ASP Conf. Ser. 234, X-ray Astronomy 2000, ed. R. Giacconi, S. Serio, & L. Stella (San Francisco, CA: ASP), 569
Robertson, I. P., & Cravens, T. E. 2003, JGR, 108, 8031
Sakai, K., Mitsuda, K., Yamasaki, N. Y., et al. 2012, in AIP Conf. Proc. 1427, *SUZAKU* 2011: Exploring the X-ray Universe: *Suzaku* and Beyond, ed. R. Petre, K. Mitsuda, & L. Angelini (Melville, NY: AIP), 342
Sanderson, A. J. R., Ponman, T. J., Finoguenov, A., Lloyd-Davies, E. J., & Markevitch, M. 2003, MNRAS, 340, 989
Schlegel, D. J., Finkbeiner, D. P., & Davis, M. 1998, ApJ, 500, 525
Shapiro, P. R., & Field, G. B. 1976, ApJ, 205, 762
Shelton, R. L. 2006, ApJ, 638, 206
Shelton, R. L., Sallmen, S. M., & Jenkins, E. B. 2007, ApJ, 659, 365
Smith, M. C., Ruchti, G. R., Helmi, A., et al. 2007a, MNRAS, 379, 755
Smith, R. K., Bautz, M. W., Edgar, R. J., et al. 2007b, PASJ, 59, S141
Snowden, S. L., Burrows, D. N., Sanders, W. T., Aschenbach, B., & Pfeffermann, E. 1995, ApJ, 439, 399
Snowden, S. L., Collier, M. R., & Kuntz, K. D. 2004, ApJ, 610, 1182
Snowden, S. L., Egger, R., Finkbeiner, D. P., Freyberg, M. J., & Plucinsky, P. P. 1998, ApJ, 493, 715
Snowden, S. L., Freyberg, M. J., Kuntz, K. D., & Sanders, W. T. 2000, ApJS, 128, 171
Snowden, S. L., & Kuntz, K. D. 2011, Cookbook for Analysis Procedures for *XMM-Newton* EPIC MOS Observations of Extended Objects and the Diffuse Background, version 4.3 (ftp://legacy.gsfc.nasa.gov/xmm/software/xmm-esas/xmm-esas.pdf)
Toft, S., Rasmussen, J., Sommer-Larsen, J., & Pedersen, K. 2002, MNRAS, 335, 799
Vikhlinin, A., & Forman, W. 1995, ApJL, 455, L109
Wall, J. V., & Jenkins, C. R. 2003, Practical Statistics for Astronomers (Cambridge: Cambridge Univ. Press)
Wang, Q. D. 1998, in The Local Bubble and Beyond, ed. D. Breitschwerdt, M. J. Freyberg, & J. Trümper (Lecture Notes in Physics, Vol. 506; New York: Springer), 503
Wang, Q. D., & Yao, Y. 2012, arXiv:1211.4834v1
Wang, Q. D., & Yu, K. C. 1995, AJ, 109, 698
Wargelin, B. J., Markevitch, M., Juda, M., et al. 2004, ApJ, 607, 596
Watson, M. G., Auguères, J.-L., Ballet, J., et al. 2001, A&A, 365, L51
Watson, M. G., Schröder, A. C., Fyfe, D., et al. 2009, A&A, 493, 339
Williams, R. J., Mathur, S., Nicastro, F., et al. 2005, ApJ, 631, 856
Yan, M., Sadeghpour, H. R., & Dalgarno, A. 1998, ApJ, 496, 1044
Yao, Y., Nowak, M. A., Wang, Q. D., Schulz, N. S., & Canizares, C. R. 2008, ApJL, 672, L21
Yao, Y., & Wang, Q. D. 2007, ApJ, 658, 1088
Yao, Y., Wang, Q. D., Hagihara, T., et al. 2009, ApJ, 690, 143
Yoshino, T., Mitsuda, K., Yamasaki, N. Y., et al. 2009, PASJ, 61, 805